SELF-CONSISTENT RATE EQUATION MODELING OF BI-FUNCTIONAL QUANTUM CASCADE STRUCTURES

A THESIS SUBMITTED TO
THE GRADUATE SCHOOL OF NATURAL AND APPLIED SCIENCES
OF
MIDDLE EAST TECHNICAL UNIVERSITY

BY

OZAN BERK BOYRAZ

IN PARTIAL FULFILLMENT OF THE REQUIREMENTS
FOR
THE DEGREE OF MASTER OF SCIENCE
IN
MICRO AND NANOTECHNOLOGY

JUNE 2023

Approval of the thesis:

SELF-CONSISTENT RATE EQUATION MODELING OF BI-FUNCTIONAL QUANTUM CASCADE STRUCTURES

submitted by **OZAN BERK BOYRAZ** in partial fulfillment of the requirements for the degree of **Master of Science in Micro and Nanotechnology Department, Middle East Technical University** by,

Prof. Dr. Halil Kalıpçılar
Dean, Graduate School of **Natural and Applied Sciences** _____

Prof. Dr. Deniz Üner
Head of Department, **Micro and Nanotechnology** _____

Assoc. Prof. Dr. Serdar Kocaman
Supervisor, **Micro and Nanotechnology, METU** _____

Prof. Dr. Alpan Bek
Co-supervisor, **Physics, METU** _____

Examining Committee Members:

Prof. Dr. Raşit Turan
Physics, METU _____

Assoc. Prof. Dr. Serdar Kocaman
Electrical-Electronics Engineering, METU _____

Assoc. Prof. Dr. Selçuk Yerci
Electrical-Electronics Engineering, METU _____

Assoc. Prof. Dr. Dinçer Gökçen
Electrical-Electronics Engineering, Hacettepe University _____

Assoc. Prof. Dr. Tahir Çolakoğlu
Physics Engineering, Ankara University _____

Date:19.06.2023

I hereby declare that all information in this document has been obtained and presented in accordance with academic rules and ethical conduct. I also declare that, as required by these rules and conduct, I have fully cited and referenced all material and results that are not original to this work.

Name, Surname: Ozan Berk Boyraz

Signature :

ABSTRACT

SELF-CONSISTENT RATE EQUATION MODELING OF BI-FUNCTIONAL QUANTUM CASCADE STRUCTURES

Boyraz, Ozan Berk
M.S., Department of Micro and Nanotechnology
Supervisor: Assoc. Prof. Dr. Serdar Kocaman
Co-Supervisor: Prof. Dr. Alpan Bek

June 2023, 70 pages

This study presents a single, self-consistent model based on the rate equations that accurately estimate the performance parameters for quantum cascade structures for both lasing operation and photodetection operation. The steps of the model are the solution of the temperature-dependent effective mass Schrödinger equation, calculation of the optical and the non-optical scattering rates between energy sub-bands, electrical and optical analysis of quantum cascade structure, and estimating the fundamental performance parameters. This model can be utilized to design bi-functional quantum cascade lasers/ photodetectors, which helps develop monolithic integration for on-chip applications. Also, with the proposed simulation tool and the aid of commercial software, a bi-functional device operating at $3 - 4\,\mu\mathrm{m}$ spectral window is designed, where the intrinsic wavelength shift is minimized while ensuring optimal performance.

Keywords: quantum cascade lasers, quantum cascade detectors, self consistent rate

equation modelling, unique design for $3 - 4\,\mu\mathrm{m}$ wavelength

ÖZ

İKİ İŞLEVLİ KUANTUM KASKAT YAPILARIN ORAN DENKLEMLERİYLE KENDİ KENDİNE TUTARLI MODELLENMESİ

Boyraz, Ozan Berk
Yüksek Lisans, Mikro ve Nanoteknoloji Bölümü
Tez Yöneticisi: Doç. Dr. Serdar Kocaman
Ortak Tez Yöneticisi: Prof. Dr. Alpan Bek

Haziran 2023 , 70 sayfa

Bu çalışmada lazer ve fotodedektör olarak çalışan kuantum kaskat yapıların temel performans parametrelerinin kestirimi için oran denklemlerini temel alan, kendi kendine tutarlı bir benzetim modeli sunulmuştur. Model, sıcaklığa bağımlı etkin-kütle Schrödinger denkleminin çözülmesi, enerji alt bantları arası optik ve optik olmayan saçılma oranlarının hesaplanması, kuantum kaskat yapının elektriksel ve optik analizi ve temel performans parametrelerinin kestirimi aşamalarından oluşmaktadır. Bu model, çip üzeri uygulamalarda yekpare entegrasyon için iki işlevli laser/dedektör yapılarının tasarımında kullanılabilir. Ayrıca, sunulan benzetim modeli ve mevcut olan başka bir ticari modelleme yazılımının yardımıyla, $3-4\,\mu\mathrm{m}$ aralığında çalışan, cihaz performansını bozmadan dalga boyu kayması azaltması sunan bir iki işlevli cihaz tasarlanmıştır.

Anahtar Kelimeler: kuantum kaskat lazerler, kuantum kaskat dedektörler,kendi ken-

dine tutarlı modelleme, $3 - 4\,\mu\mathrm{m}$ dalgaboyu için özgün tasarım

To my best friends Yami,Deniz and my family

ACKNOWLEDGMENTS

I would like to express my sincere gratitude and appreciation to several individuals who have played an instrumental role in the completion of my Master's thesis. Their support, guidance, and encouragement have been invaluable throughout this journey.

First and foremost, I would like to extend my deepest thanks to Prof. Serdar Kocaman and Prof. Alpan Bek for their unwavering commitment to academic excellence and his invaluable guidance throughout the research process. Their profound knowledge, insightful suggestions, and constructive feedback have significantly shaped the quality and direction of this thesis. I am truly grateful for their expertise and dedication.

I would also like to express my heartfelt appreciation to my dear friend Onur. His unwavering support, encouragement, and countless discussions have been instrumental in keeping me motivated and focused on my research. His insightful perspectives and constructive criticisms have helped me refine my ideas and improve the overall quality of this work. I am truly fortunate to have him as a friend and colleague.

Furthermore, I would like to extend my gratitude to my colleagues for their constant support and collaboration throughout this academic endeavor. Their valuable insights, constructive discussions, and willingness to share their knowledge have enriched my research and broadened my understanding of the subject matter. I am grateful for their camaraderie and teamwork, which have made this journey both intellectually stimulating and enjoyable.

Lastly, I would like to express my deepest appreciation to Deniz. She has provided assistance and encouragement during the course of this research. Her contributions have been significant and have helped shape this thesis into what it is today.

TABLE OF CONTENTS

LIST OF TABLES

TABLES

LIST OF FIGURES

FIGURES

LIST OF ABBREVIATIONS

ISB	Intersubband
QCL	Quantum cascade laser
QCD	Quantum cascade detector
QCLD	Quantum cascade laser/detector
QWIP	Quantum well infrared photodetector
THz	Terahertz
NIR	Near infrared
FIR	Far infrared
LO	Longitudinal optic
IFR	Interface roughness
SL	Superlattice
EMC	Ensemble Monte Carlo
NEGF	Non-equilibrium Green's function
MQW	Multi quantum well
FDM	Finite difference method
RK-4	Runge-Kutta method
RKF	Runge-Kutta-Fehlberg method

CHAPTER 1

INTRODUCTION

1.1 Motivation and Problem Definition

Due to the increasing demand for high-speed communication and next-generation wireless systems, there is a need for advancements in the transmission capacities of communication systems. Photonic integrated circuits can replace traditional copper-based technology. Photonic integrated circuits (PICs) are promising and in demand since they offer higher speed data transfer rates, more energy efficiency, and compactness when compared to traditional electronic circuits.

Silicon is a particularly attractive material for PICs due to its compatibility with existing complementary metal-oxide-semiconductor (CMOS) fabrication processes widely used in the semiconductor industry. It is possible to realize passive or active devices such as waveguides, modulators, photodetectors, optical couplers, and splitters on a Si-based PIC. Also, integrating III-V material-based active devices onto Si-based PICs is commonly used.

In photonic integrated circuits, transmitters (laser) and receivers (photodetector) are two key components. Using different types of laser and detector in a single chip introduces difficulties and design complexity in fabrication. Also, it needs strict alignment tolerances. Using a single epilayer for both laser and photodetection enables the fabrication of well-functioning and robust photonic integrated circuits.

A specific type of laser, based on intersubband transitions, called "Quantum cascade laser (QCL)," can be used as a transmitter in photonic integrated circuits. Intersubband transitions were first presented by Kazarinov and Suris in 1971 [1]. Their study

showed amplification of light is possible between two intersubband states. Due to insufficient manufacturing technology, until the early 1990s, it was not possible to manufacture and demonstrate the first quantum cascade laser. Faist and Capasso proposed the first quantum cascade laser successfully in 1994 [2]. Many studies followed their work. First QCL was on near to far infrared region, following studies extended to the terahertz (THz) region. A quantum cascade structure can be utilized for also photodetection. The idea of using quantum cascade structures as photodetectors were presented by Hofstetter et.al [3]. But the primitive design was not a functional device, which shows poor detector performance. In the following studies, improved quantum cascade detectors were introduced. This enables the generation and detection of the same wavelength using the same epilayer material; it allows monolithic integration for on-chip applications. However, obtaining the same wavelength for both laser and detector is challenging due to the intrinsic nature of quantum cascade structures.

Although open source and commercial QCL design and simulation programs exist, QCD simulation tools are not widely available since QCDs are relatively newer devices than QCLs and have not drawn much attention than QCLs. For obtaining accurate results, it is not directly possible to simulate QCDs within a QCL simulation framework because photocurrents in QCDs are much smaller than the pump currents of QCLs. [4]. In general, QCL simulation tools do not include the irradiation of the designed structure since they focus on estimating some fundamental laser parameters such as population inversion, the gain of the active region for stimulated emission, threshold current, etc. Also, for dark current calculations, some mechanisms like impurity scattering, resonant tunneling current, etc. are not included which is negligible for QCL modeling but important for accurate QCD modeling.

1.2 Proposed Method and Thesis Contribution

This study aims to fill the gap in QCL and QCD modeling and provide an open-source simulation tool for modeling bi-functional quantum cascade structures.

The proposed simulation tool solves the effective mass Schrödinger equation and calculates the transition rates between energy sub-bands based on Longitudinal optical

phonon (LO-Phonon) and Interface Roughness (IFR) scattering. Based on the optical dipole matrix element between states and state lifetimes, it returns a figure of merit indicating the lasing probability and fundamental detector performance parameters.

Also this study proposes a design of a bi-functional quantum cascade laser and detector (QCLD) which offers reduced intrinsic wavelength shift between QCL and QCD. For further studies, the proposed simulation tool can be used for designing various QCLDs and the designed structure can be used as a source and receiver while designing a photonic integrated circuit for on-chip applications. Finally, if other aspects of the design steps such as waveguide design and thermal design are also studied, designed QCLD can be grown in our lab.

1.3 The Outline of the Thesis Chapter Definitions

Chapter 1 gives the motivation and defines the problem while briefly introducing the proposed model and thesis contribution.

Chapter 2 gives information about QCLs, QCL material systems, and commonly used QCL modeling techniques.

Chapter 3 explains the QCDs and compares QCDs with another type of photodetectors based on intersubband transitions, quantum well infrared photodetectors (QWIP). Also, presents available material systems for the fabrication of QCDs. QCD modeling techniques are given at the end of Chapter 3.

Chapter 4 gives the effective carrier scattering mechanisms that exist in quantum cascade structures.

Chapter 5 gives a detailed explanation of the proposed simulation framework.

Chapter 6 provides some simulation outputs, starting from simple structures to more complex ones such as the evaluation of longitudinal optical phonon scattering in a single quantum well simulation of QCL and QCD.

Chapter 7 presents a bi-functional device design for $3-4\,\mu\mathrm{m}$ window with design considerations.

Chapter 8 concludes the study and discusses future work.

CHAPTER 2

QUANTUM CASCADE LASERS

A specific type of laser based on intersubband transitions are called "Quantum Cascade Laser (QCL)". In this chapter, quantum cascade lasers are explained, starting from interband and intersubband transitions, then active region of QCL, commonly used material systems, and modeling techniques.

2.1 Interband vs Intersubband Transitions

If there exists a bandgap between two energy states, curvatures of these states in the E-k diagram (dispersion diagram) are oppositely signed and transitions between these states are called interband transitions, since transitions occur from valence band to conduction band, or vice versa. These transitions generally end up with the generation or recombination of carriers.

In contrast, if two energy states are in the same band (conduction band or valence band), their curvature in the dispersion curve is similar. If transitions take place within the same band, these types of transitions are called intersubband transitions.

Figure 2.1 illustrates the interband and intersubband transitions and their representation in the E-k diagram.

The existence of the bandgap limits the transition energy in interband transitions. Energy values for transitions that are lower than bandgap are forbidden. Therefore material system limits the energy of transitions. On the other hand, transition energies for intersubband transitions can be engineered by adjusting the quantum well thickness, which enables working over a wide energy range.

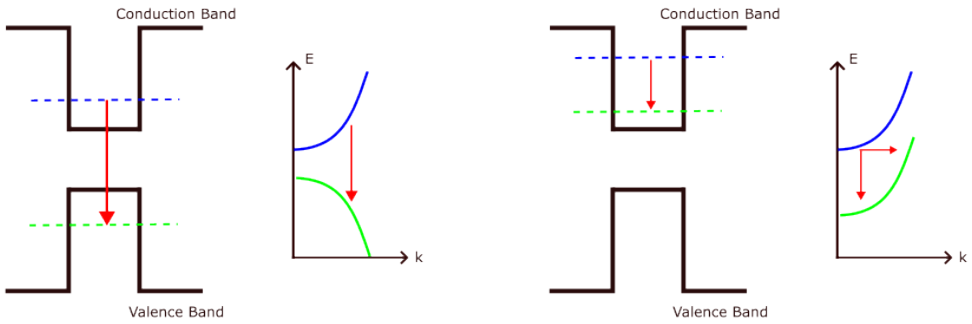

(a) (b)

Figure 2.1: (a) Interband and (b) Intersubband transitions in a heterojunction quantum well

2.2 Active Region of Quantum Cascade Laser

If layers (layer thickness are in order of a few angstroms to a few nanometers) of two or more different materials (or materials with different lattice constants) are brought together, artificially engineered structures can be formed, and these structures are called superlattices. A typical superlattice energy diagram is illustrated in Figure 2.2

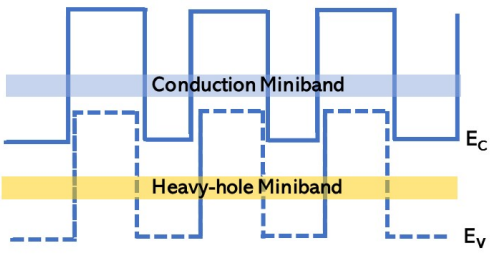

Figure 2.2: Conduction and valence band energy diagram of a superlattice, redrawn after [5]

The energy diagram bends if an electric field is applied to a superlattice structure. By controlling the amount of applied E-Field, it is possible to locate the ground state of the well close to the excited states of the following wells. Figure 2.3 shows a superlattice under e-field [1].

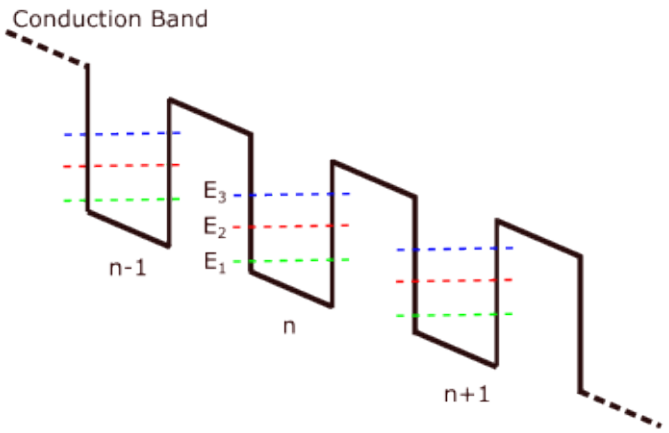

Figure 2.3: Conduction band energy diagram of a superlattice under E-Field, redrawn after [1]

However, this type of structure is hard to realize since the structure operates under unstable e-field regions of negative differential resistance [5]. To implement a laser based on intersubband transitions electrical stability at the operating point is a must, population inversion should be achieved, and the resultant gain should overcome waveguide and other active region losses [5]. A simple superlattice under the e-field is not enough to meet the requirements mentioned above. A special design is needed, and the first design which accomplishes all of these requirements was introduced by Jerome Faist and Federico Capasso [2]. Their proposed structure consists of 3 building blocks: Injector region, gain region, and relaxation region. Active region consists of a periodic arrangement of these 3 building blocks. Figure 2.4 illustrates the injector, gain, and active region.

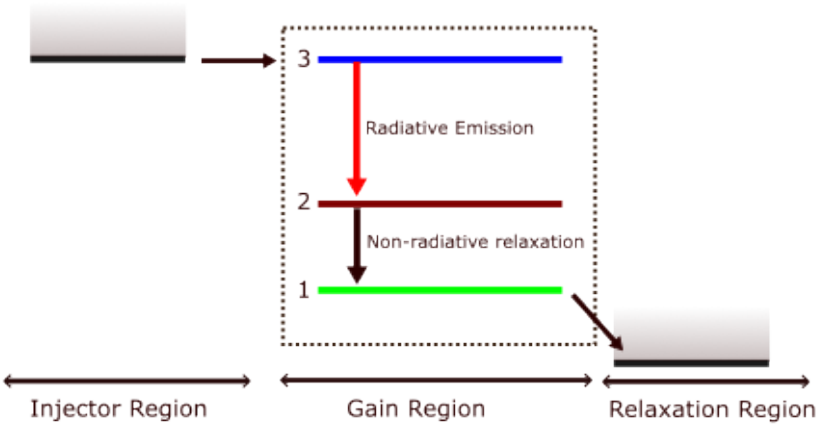

Figure 2.4: Building blocks of a QCL

The gain region is the region where the population inversion is achieved and maintained. Energy levels responsible for laser transition are located inside the gain region. The injection region is responsible for stepping-up energy level compared to the band edge and injecting the electron onto the gain region by resonant tunneling [6]. The relaxation region extracts the electron from the gain region and in fact, it behaves as an injector of the following gain region. The presence of injection and relaxation regions also comes with advantages. They prevent the formation of electrical domains, reduce the applied e-field to the period, and maintain the population inversion by blocking the electron escape from the upper lasing level in the gain region [5, 6, 7].

2.3 QCL Material Systems

When two different types of material are brought together (called heterojunction), their energy bands interact. Under zero bias, energy bands of different materials relatively align to ensure the continuity of the Fermi level. At the interface of two different materials, the discontinuity of energy bands due to that relative alignment is called band offset. Heterojunction interfaces can be classified into three types. Type-I heterojunction is formed when the conduction band of the first material is greater than the second one, while the valence band of the second material is greater than the first one. Type-I heterojunctions are also referred to as straddling gap heterojunctions.

In Type-II heterojunctions (staggered gap), both the conduction band and valence band of the second material are lower than the first one, but the conduction band of the second material is higher than the valence band of the first material. If the first material's conduction band and valence band are higher than the second material's and the conduction band of the second material is located below the valence band, the formed heterojunction is called Type-III (broken gap).

Figure 2.5 illustrates three different types of semiconductor heterojunction band structures.

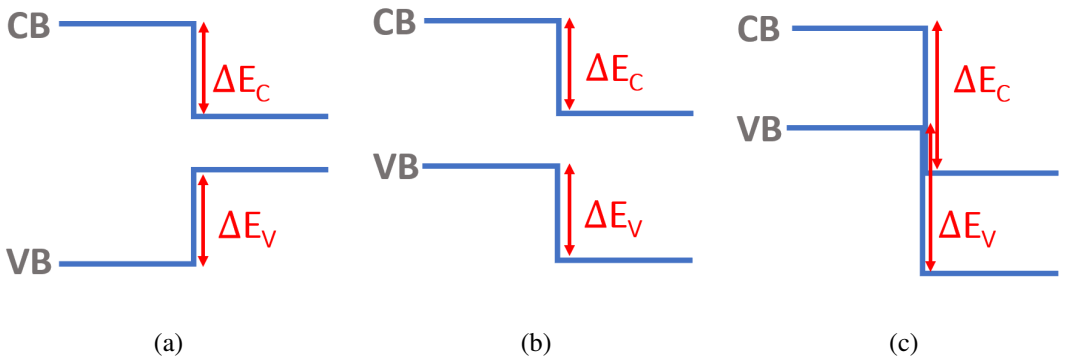

Figure 2.5: Different band alignments in semiconductor heterojunctions. (a) Type-I, (b) Type-II, (c) Type-III

Quantum cascade lasers are Type-I structures, and their transition energy is limited by conduction band discontinuity and also influenced by electron effective mass. Table 2.1 gives examples of material systems used for fabricating short-wavelength QCLs, their conduction band discontinuity, achieved wavelength, and characteristic temperature of operation.

Obtaining smaller photon energy than the conduction band offset is due to the thermal escape of electrons to continuum states or states in the other valleys, as illustrated in Figure 2.6. When the thickness of the quantum well decreases, the energy of the emitted light between energy subbands increases. The leakage of carriers to the indirect valleys becomes more pronounced. In fact, the efficiency of lasers operating in this range of wavelengths is mainly hindered by carriers escaping into the surrounding environment due to thermal activation, scattering of carriers towards different

Table 2.1: Different material systems used for short-wavelength QCLs

Material System	$\Delta E_c(meV)$	$E_{photon}\,(meV)$	$\lambda_{photon}\,(\mu m)$	Temperature (K)	Reference
$GaAs/Al_{0.33}Ga_{0.67}As$	297	107	11.5	96	[8]
$GaAs/Al_{0.33}Ga_{0.67}As$	297	120	9.3	166	[9]
InGaAs/AllnAs	520	108	11.5	170	[10]
InGaAs/AllnAs	520	138	9	190	[11]
InGaAs/AllnAs	520	159	7.8	164	[12]
InGaAs/AllnAs	520	238	5.2	114	[13]
$In_{0.7}Ga_{0.3}As/Al_{0.6}In_{0.4}As$	800	288	4.3	188	[14]
$In_{0.7}\,Ga_{0.3}As/Al_{0.6}In_{0.4}As$	800	355	3.49	85	[15]
$In_{0.73}Ga_{0.27}As/AlAs$	1000	326	3.8	143	[16]
$In_{073}\,Ga_{0.27}As/AlAs(Sb)$	1600	375	3.3	101	[17]
$In_{0.73}Ga_{0.27}As/AlAs(Sb)$	1600	344	3.6	116	[17]
InAs/AISb	2100	375	3.3	200	[18]

valleys, and reabsorption of carriers within the extraction region. Additionally, developing lasers that emit at these wavelengths requires the utilization of very thin quantum wells, demanding precise management of interface roughness and material strain during the growth process. As layers get thinner, small surface irregularities at the layer interface lead to increased losses and scattering.

Another limitation of QCLs is heating at high power levels. Typically, as the temperature of the device increases, carrier scattering rates tend to increase, which limits the performance of the device. Therefore, to maintain stable operation, generated heat must be effectively removed by proper thermal management. Also, at high power levels, non-linear effects arise, and they limit the maximum achievable output power.

In conclusion, while designing QCLs, there are trade-offs between power, reliability, and efficiency.

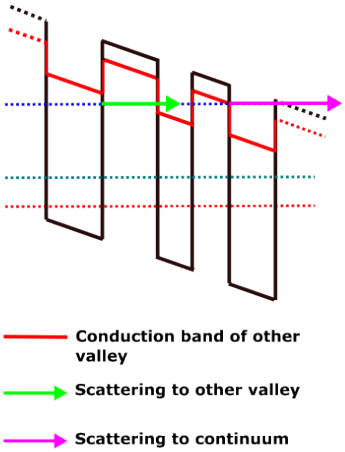

Figure 2.6: The escape of electrons onto continuum or other valleys

2.4 QCL Modelling Techniques

Modeling quantum cascade lasers mainly consists of three modeling steps:

1. Numerically solving Schrodinger-Poisson Equation to obtain the energy levels and wave functions will be inputs of the carrier transport model.
2. Carrier transport modeling to investigate the physical process and obtain key performance parameters.
3. Optical resonator modeling to obtain aspects of the cavity.

Figure 2.7 shows three main modeling steps.

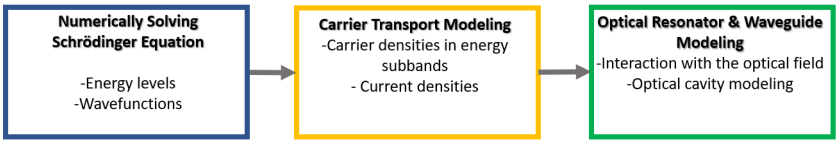

Figure 2.7: Main steps of QCL modeling

Detailed information on numerically solving Schrodinger Equation is provided in Chapter 5. This chapter will investigate different approaches to carrier transport

modeling from the literature, such as the rate equation model, ensemble Monte Carlo (EMC) model, and non-equilibrium Green's function (NEGF).

While selecting the carrier transport model, like in every computational problem, there is a trade-off between complexity and accuracy. It is possible to classify carrier transport models into two groups: semi-classical and fully quantum mechanical models. Also, another classification of the models can be done as empirical and self-consistent models.

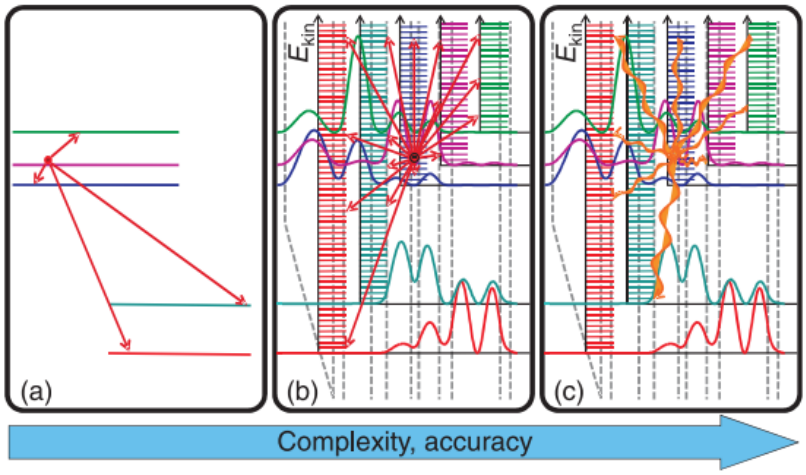

Figure 2.8: Comparison of (a) Rate Equation Model, (b) Ensemble Monte-Carlo (EMC) Method, and (c) NEGF for QCL modeling [19]

Figure 2.8 illustrates the complexity of three different carrier transport models. (a) the rate equation approach is the simplest but most widely used model in the literature. (b) is the Ensemble Monte Carlo model (EMC). The EMC method is more accurate than the simple rate equation model. (c) the Non-Equilibrium Green's Function approach is the most accurate while being the most complex.

2.4.1 Rate Equation Model

The rate equation model aims to investigate the carrier transport process by finding the evolution of electron and photon densities by a system of coupled differential equations. This approach considers electron injection-transportation-relaxation, stimulated/spontaneous emission, absorption, and scattering processes. Using rate equa-

tion models is advantageous since it is numerically efficient, intuitive, and provides important insights into the behavior of the structure [20].

In the rate equation model, injectors are represented as a single energy level, and in the active region, it is assumed that there are three states. Figure 2.9 shows the active region with injectors.

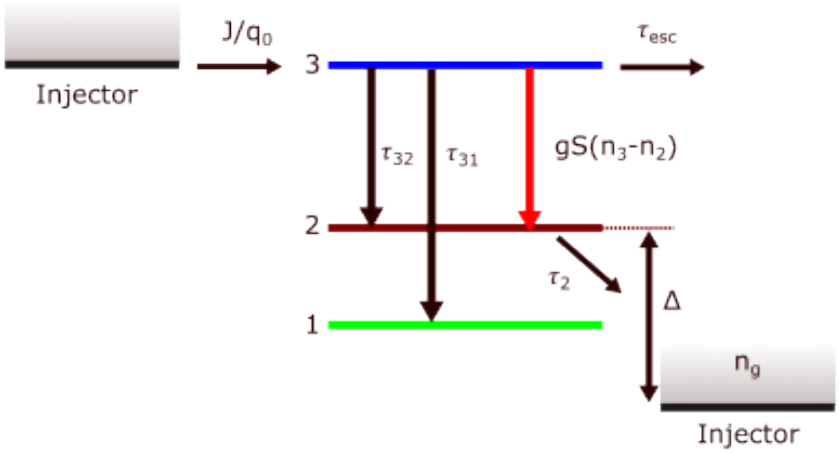

Figure 2.9: Three-level modeling of the active region with single energy level injectors, redrawn after [5]

Lasing occurs between 3rd and 2nd states. J/q_0 is the electron injection rate from the injector's ground rate onto 3rd energy level. τ_{ij}^{-1} is the total scattering rate from ith state onto jth state. Lifetime of 3rd state is expressed by Equation 2.1 :

$$\tau_3{}^{-1} = \tau_{32}{}^{-1} + \tau_{31}{}^{-1} + \tau_{esc}{}^{-1} \tag{2.1}$$

The electron escape rate onto the continuum is represented with a rate of τ_{esc}^{-1} . Change rates with respect to time in the active region can be expressed as:

$$\frac{dn_3}{dt} = \frac{J}{e} - \frac{n_3}{\tau_3} - S_{g_c}(n_3 - n_2) \tag{2.2}$$

$$\frac{dn_2}{dt} = \frac{n_3}{\tau_{32}} + S_{g_c}(n_3 - n_2) - \frac{n_2 - n_2^{therm}}{\tau_2} \tag{2.3}$$

$$\frac{dS}{dt} = \frac{c}{n_{\tau \text{efr}}} \left[(g_c (n_3 - n_2) - \alpha_{tot}) S + \beta \frac{n_3}{\tau_{sp}} \right] \tag{2.4}$$

Where n_2^{therm} is the population of 2nd energy level at thermal equilibrium, and it is approximately equal to:

$$n_2{}^{therm} = n_g exp\left(-\Delta / kT\right) \tag{2.5}$$

$$\Delta = \mathrm{E}_{fermi}^{injector} - \mathrm{E}_2 \tag{2.6}$$

$$g_c = \Gamma \frac{4\pi \mathrm{e}^2}{\epsilon_0 n_{refr} \lambda} \frac{{z_{32}}^2}{2\gamma_{32} L_p} \tag{2.7}$$

With the assumption of $\tau_{sp} \gg \tau_3$ below the lasing threshold, dn_i/dt values, and S are equal to zero.

Since n_3 is pumped by the injector at a rate of J/q_0,

$$n_3 = J\tau_3 / e \tag{2.8}$$

$$\Delta \mathrm{n} = n_3 - n_2 \tag{2.9}$$

By combining Equation 2.8 and Equation 2.9, population inversion can be found as in Equation 2.10.

$$\Delta \mathrm{n} = \frac{J\tau_3}{e} \left(1 - \frac{\tau_2}{\tau_{32}} \right) - n_2{}^{therm} \tag{2.10}$$

In Equation 2.10 above, τ terms can be grouped and written as follows:

$$\tau_{eff} = \tau_3 \left(1 - \tau_2 / \tau_{32}\right) \tag{2.11}$$

Then, Equation 2.10 becomes:

$$\Delta n = \frac{J\tau_{eff}}{e} - {n_2}^{therm} \tag{2.12}$$

Following deductions can be made from 2.12 as follows:

- $\tau_{eff} > 0$, population inversion exists ($\tau_2 < \tau_{32}$).
- If $\tau_{32} \gg \tau_2$ then τ_{eff} is approximately equal to τ_3 .

At the threshold:

$$\alpha_{tot} = g_c \Delta n \tag{2.13}$$

Then, threshold current density can be expressed as:

$$J_{th} = e\frac{\alpha_{tot}/g_c + {n_2}^{therm}}{\tau_{eff}} \tag{2.14}$$

Then, by interting Equation 2.7 into Equation 2.14 :

$$J_{th} = \frac{1}{\tau_{eff}} \left[\frac{\epsilon_0 n_{\tau \text{efr}} L_p \lambda \left(2_{\gamma 32}\right)}{4\pi \text{e} \Gamma {z_2}^{32}} \alpha_{tot} + e{n_2}^{therm} \right] \tag{2.15}$$

For $J > J_{th}$, Δn becomes constant, and as J increases, S increases linearly.

$$\frac{dP}{dI} = N_p h V \alpha_{m,1} \frac{dS}{dJ} = \frac{N_p h v}{e} \frac{\alpha_{m,1}}{\alpha_{tot}} \frac{\tau_{eff}}{\tau_{eff} + \tau_2} \tag{2.16}$$

Equation 2.16 gives the slope efficiency where $\alpha_{m,1}$ is the loss of the front mirror.

Figure 2.10 illustrates the population inversion and photon flux versus injected current. By analyzing Equation 2.15 and Equation 2.16 , a highly efficient laser with a low threshold current can be designed by considering the following parameters:

- Large upper to lower state lifetime ratio i.e. large τ_{32}/τ_2.

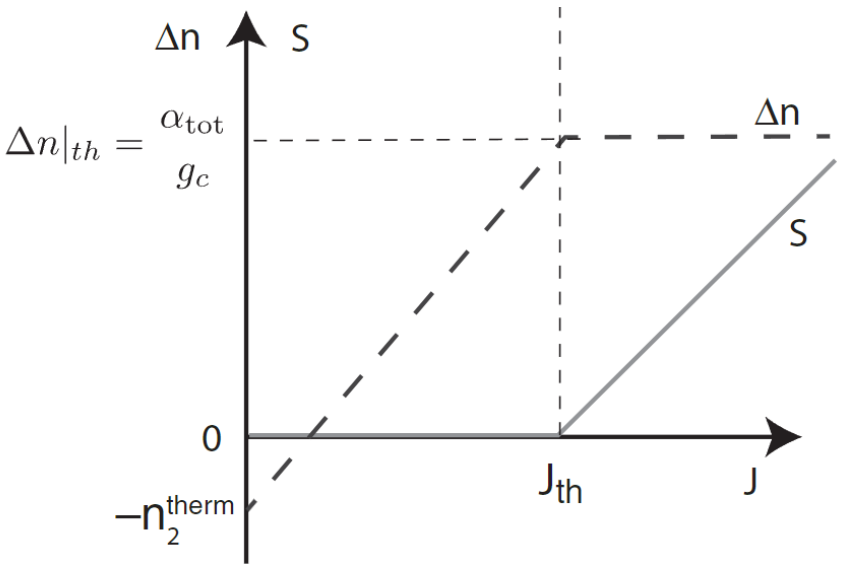

Figure 2.10: Injected current density vs population inversion and photon flux [5]

- Low $\alpha_{waveguide}$.
- Small γ_{32}.
- High τ_3.

It is possible to group rate equation models as empirical rate equation model and self-consistent rate equation model. The empirical rate equation model relies on phenomenological equations and empirical parameters such as experimentally measured scattering rates. It does not take into account the detailed microscopic processes.

In the self-consistent rate equation model, intersubband scattering rates, i.e. ${\tau_{ij}}^{-1}$ values are determined based on material parameters (for example effective mass) and do not rely on any experimentally measured lifetimes [4]. In the self-consistent rate equation model, generally optical cavity field is ignored, therefore, they model the behavior of the structure until population inversion is achieved. A detailed explanation of the self-consistent rate equation model will be explained in the following sections.

2.4.2 Ensemble Monte Carlo Method (EMC)

The Boltzmann equation governs the carrier transport between energy states in a system consisting of multiple quantum wells [21].

$$\mathrm{d}_t f_{i\mathbf{k}} = \sum_j \sum_{\mathbf{k}'} \left(W_{j\mathbf{k}',i\mathbf{k}} f_{j\mathbf{k}'} - W_{i\mathbf{k},j\mathbf{k}'} f_{i\mathbf{k}} \right) \tag{2.17}$$

where the overall scattering rate can be expressed by the sum of different scattering mechanisms:

$$W_{i\mathbf{k},j\mathbf{k}'} = \sum_m W^{(m)}_{i\mathbf{k},j\mathbf{k}'} \tag{2.18}$$

$f_{i\mathbf{k}}$ is the state occupancy probability at time t. EMC method is utilized for solving Equation 2.18 numerically. Simulations are conducted until convergence is reached. Simulation time t_{sim}, consists of δ_t time steps that provide precise numerical resolution. Thanks to the periodicity of the quantum cascade structures, a representative part of the structure consisting of a few periods is considered in EMC simulations to reduce the computational effort. Also, to reduce the number of iterations, initial state occupancy probabilities can be calculated by Maxwell-Boltzmann distribution:

$$f_i^{\mathrm{MB}} \left(E_{i\mathbf{k}} \right) = \exp \left[- \left(E_{i\mathbf{k}} - E_i^{\mathrm{F}} \right) / \left(k_{\mathrm{B}} T_i \right) \right] \tag{2.19}$$

An example of EMC algorithm is given in Figure 2.11.

After finding the number of electrons that scatter from one period to other neighbor periods, Δ_N, and the number of electrons in the central period, N_e, in a time step Δ_t , for sheet doping density per period is n^s, the current density can be calculated as follows:

$$J = \frac{\Delta_N e n^{\mathrm{s}}}{\Delta_t N_c} \tag{2.20}$$

2.4.3 Non-Equilibrium Green's Function (NEGF) Method

Quantum cascade devices are in the nanometer scale. At carrier transport in this scale, quantum effects are significant. To model precisely and accurately a device in nanometer scale, a fully quantum mechanical carrier transport model is required. The

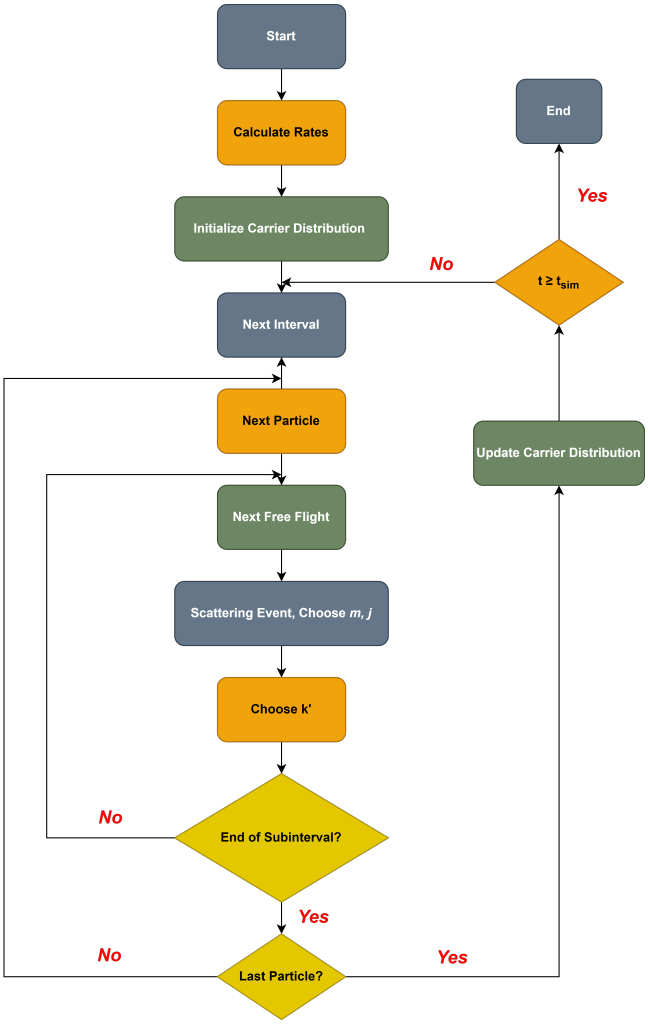

Figure 2.11: Flowchart of EMC algorithm, redrawn after [4]

Non- Equilibrium Green's Function (NEGF) method provides a theoritical framework for quantum transport at the nanometer scale devices such as quantum dots, nanowires and quantum cascade structures, etc. NEGF method allows the calculation of some transport properties such as current-voltage characteristics, density of states, etc.

Some non-equilibrium effects such as carrier heating, energy relaxation, and velocity overshoot, which are important for accurately modeling QCLs can be handled with NEGF method. In contrast, rate equation models and EMC methods assume thermal equilibrium or average carrier distributions, which may not capture the full dynamics of carrier transport in QCLs.

While the NEGF method offers higher accuracy, it requires more computational com-

plexity when compared to other carrier transport models. Also, higher computational times are required, which makes application of NEGF method unpractical in some cases where multiple iterations during the design is needed such as optimization problems.

CHAPTER 3

QUANTUM CASCADE DETECTORS

Intersubband transition in multi-quantum well structures (MQW) was observed by West et.al. in 1985 first [22]. Using the intersubband transitions for the detection of incident radiation was introduced in 1987, and the proposed structure was the first demonstration of photoconductive quantum-well infrared photodetectors. Following the fabrication of the first quantum cascade lasers and advancements in QCLs, the idea of using quantum cascade structures as photodetectors were proposed [3]. A Quantum cascade detector is a photovoltaic photodetector that enables intersubband (ISB) transitions.

3.1 QWIP vs QCD

Quantum well infrared photodetectors (QWIPs) and QCDs have similar properties. Both of them are unipolar i.e. current is generated due to electrons only, they both use ISB transitions for the detection of incident light and since LO phonon scattering is utilized in QWIPs and QCDs they offer fast operation [19]. Figure 3.1 illustrates the operation of QWIP and QCD.

Besides their similar properties, QWIPs and QCDs have some differences. In general, QWIPs operate in photoconductive mode which needs to be biased where QCDs can operate under zero bias since they are in photovoltaic mode [23]. Therefore, in comparison with QWIPs, QCDs have very low dark current.

When QCDs are compared to QWIPs, QCDs have some advantages over QWIPs. The design complexity of QCDs is higher than QWIPs, which offers more degree

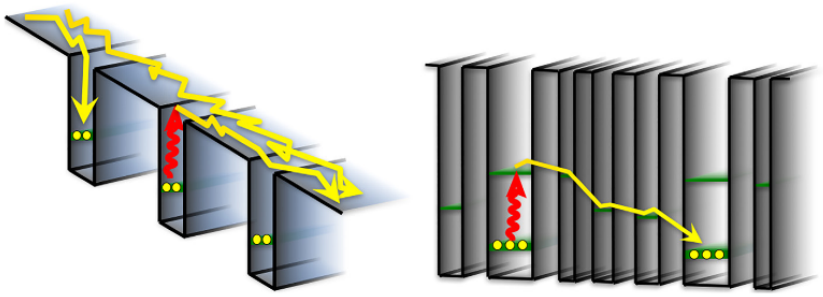

Figure 3.1: Illustration of operations of QWIP and QCD respectively [19]

of freedom while designing [19]. Therefore, they can be tailored to operate over a wide range in the electromagnetic spectrum, providing versatility and suitability for spectroscopic applications. They can reach high speeds of operation and they can operate at room temperature without a need for cooling. Also, QCDs exhibit low noise characteristics. On the other hand, the fabrication process for QCDs is more complex compared to QWIPs, and precise control is needed when fabricating QCDs. QCDs have a narrow field of view, and their quantum efficiency is lower compared to QWIPs. As the operation wavelength increases, the performance of QCDs degrades. QCD technology is relatively new than QWIP technology; therefore QCDs have limited maturity, and they are commercially less available.

3.2 Material Systems

QCL material systems can be adapted for QCD designs. Table 3.1 and Figure 3.2 from [19] gives some examples of materials systems used for the design of short wavelength QCDs from the literature.

Table 3.1: Different material systems used for short-wavelength QCDs

Material System	$\Delta E_c(meV)$	$E_{transition}\,(meV)$	$\lambda(\mu m)$	Reference
$GaAs/AlAs$	1110	550	2.25	[24]
$ln_{0.53}\,Ga_{0.47}As/Al_{0.48}\,ln_{0.52}\,As$	520	320	3.87	[25]
$In_{0.61}Ga_{0.39}As/Al_{0.55}In_{0.45}As$	610	319	3.87	[25]
$GaAs/In_{0.73}Ga_{0.27}As$	1000	326	3.8	[24]

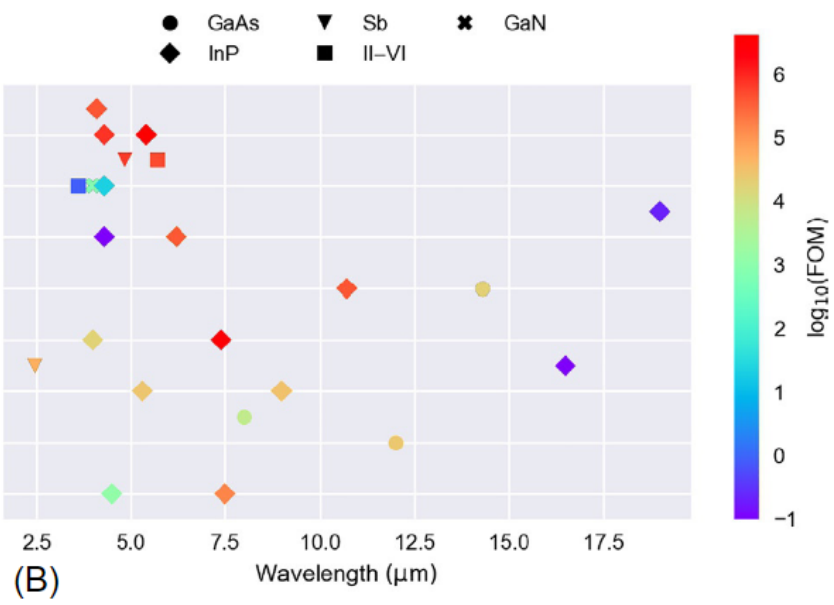

Figure 3.2: Material systems used for fabrication of QCDs and corresponding wavelength ranges [19]

3.3 Modeling Techniques

In principle, QCD modeling is similar to QCL modeling, which is explained in Chapter 2. First, the Schrödinger equation must be solved to find wavefunctions and energy eigenstates. Then, carrier transport is modeled to obtain the key performance parameters of the detector. However, the direct application of QCL models onto QCD structure is not accurate since currents (even under radiation) in QCDs are much smaller than the pumping currents of QCLs [19]. For dark current calculations of QCDs, the resulting current densities in an irradiated design are too small. All possible components (tunneling current and various scattering mechanisms, which are generally ignored while modeling QCLs) which contribute to the current must be considered. Therefore, direct application of QCL carrier transport models to QCDs is not possible and would not be accurate.

Since QCDs are relatively immature devices than QCLs, there are fewer QCD models available in the literature. For the carrier transport in QCDs, rate equation models [26, 27, 28], EMC [4, 29, 30], and NEGF models [31] are presented in the literature.

Figure 3.3 gives an overview of self-consistent rate equation modeling of quantum cascade detectors.

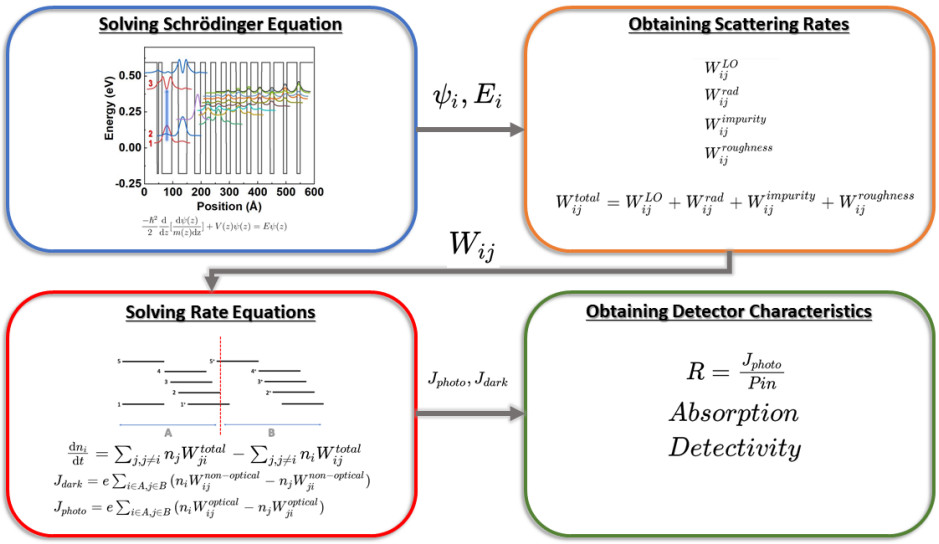

Figure 3.3: Self-consistent rate equation modeling of quantum cascade detectors

Effective mass Schrödinger Equation is solved numerically, and wavefunctions and energy levels are obtained. $W_{i,j}$ is the mean scattering rate per electron from subband i to subband j. With energy levels, wavefunctions, and some material parameters, scattering rates will be calculated. $W_{i,j}$ consists of optical and non-optical parts. The non-optical process is due to scattering by phonons, other electrons, interface roughness, impurities, etc. The optical term stands for photon absorption or emission. For dark conditions, the optical term is neglected. The dominant non-optical scattering process in quantum cascade detectors is LO phonon scattering, but other items also must be considered for accurate calculation. For the calculation of current in quantum cascade detectors, the density of electrons in each sub-band must be calculated first. Carrier dynamics are also affected by the next neighbor period's states. Assuming that electron densities are periodically the same with the structure and interaction between wavefunctions are only with the nearest neighbor period and thanks to the translational symmetry of the structure, the number of equations to be solved can be reduced.

Before solving the rate equations, two assumptions are made:

- In each period, sum of electron densities in each state is equal to dopant density.
- At steady state $dn_i/dt = 0$.

After, there are N non-linear differential equations and they will be solved by an iterative process. In the first iteration, the density of electrons will be selected as their thermal equilibrium value, and scattering rates between subbands (i.e $W_{i,j}$) will be calculated with respect to that values. After each iteration, electron densities are calculated and given as input to the differential equation system. Electron densities will converge after some number of iterations. Calculations will be finished when convergence is reached. To calculate current density, a plane between two neighboring periods will be selected as a reference plane. If the difference between forward and backward current densities is taken, the total current density can be calculated, and detector characteristics can be obtained with this information.

CHAPTER 4

CARRIER SCATTERING MECHANISMS IN QUANTUM CASCADE STRUCTURES

An electron or a hole moves in an ideal crystal lattice without any defects, it will maintain its movement in that state until infinity. In practice, the charge carrier changes its state due to defects and imperfections and this event is called as carrier scattering. From the quantum mechanical perspective, in time-dependent perturbation theory, Fermi's Golden Rule formulates the scattering between states due to a small perturbation. Transition rate from an initial state $|i\rangle$, with an energy E_i to a final state $|f\rangle$, with an energy E_f under time-dependent perturbation H' can be expressed as follows:

$$\mathrm{W}i \rightarrow f = \sum_{f} \left| f \left| \widetilde{H} \right| i \right|^2 \delta \left(E_f - E_i \right) \tag{4.1}$$

In Equation 4.1, $\left| f \left| \widetilde{H} \right| i \right|$ term represents the matrix element of perturbation between state $|i\rangle$ and state $|f\rangle$.

4.1 Longitudinal Optical Phonon Scattering

$$W_{if-tot}^{LO} = W_{if-emission}^{LO} - W_{if-absorption}^{LO} \tag{4.2}$$

Figure 4.1a shows various type of scatterings and Figure 4.1b shows LO-phonon scattering in E-k diagram

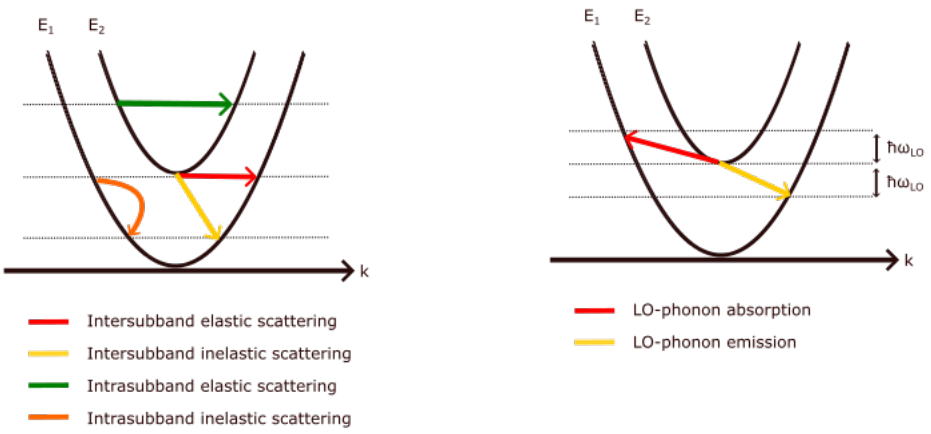

(a) (b)

Figure 4.1: LO-phonon emission and absorption in E-k diagram

4.1.1 Scattering due to LO-Phonon Absorption

In case of scattering due to LO-phonon absorption from an initial state $i|k_i>$ to final state $f|k_f>$, at T=0 K with initial and final wavevectors k_i and k_f respectively, can be expressed as:

$$\mathrm{W}_{i\to f} = \frac{m^* e^2 \omega_{LO}}{2\hbar\varepsilon_p} \sum_f \int_0^{2\pi} d\theta \frac{I^{ij}(Q)}{Q} \tag{4.3}$$

where

$$Q = \left(k_i^2 - k_f^2 - 2k_i 2k_f cos\theta\right)^{\frac{1}{2}} \tag{4.4}$$

$$k_f^2 = k_i^2 + \frac{2m^*}{\hbar^2}\left(E_i - E_f - \hbar\omega_0\right) \tag{4.5}$$

$$\epsilon_p^{-1} = \epsilon_\infty^{-1} - \epsilon_s^{-1} \tag{4.6}$$

$$I^{ij}(Q) = \int dz \int dz' \chi_i(z)\chi_f(z) e^{-Q|z-z'|} \chi_i\left(z'\right)\chi_f\left(z'\right) \tag{4.7}$$

In the equations above, m^* is electron effective mass, e is the unit charge, ω_{lo} is LO-phonon frequency, e_∞ is high-frequency relative permittivity, ϵ_s is static relative permittivity. To further simplify,k_f is assumed to be zero. Then,

$$Q = k_i \tag{4.8}$$

where

$$k_i = \left[-\frac{2m^*}{\hbar^2} \left(E_i - E_f - \hbar w_{L0} \right) \right]^{\frac{1}{2}} \tag{4.9}$$

and Equation 4.3 becomes:

$$\mathrm{W}i \rightarrow f = \frac{m^* e^2 \omega_{LO} \pi}{\kappa^2 \varepsilon_p} \frac{I^{if}(k_i)}{k_i} \tag{4.10}$$

To obtain the scattering rate due to LO-phonon absorption at non-zero temperature, Equation 4.10 is multiplied by:

$$1 + n = \left[exp \left[\frac{\hbar wLO}{kT} \right] - 1 \right]^{-1} + 1 \tag{4.11}$$

where n is the thermal population of LO-phonons.

4.1.2 Scattering due to LO-Phonon Emission

In case of scattering due to LO-phonon emission from an initial state $i|k_i>$ to final state $f|k_f>$, at T=0 K, Equation 4.3 and 4.4 holds. However, in the case of LO-phonon emission,

$$k_f^2 = k_i^2 + \frac{2m^*}{\hbar^2} \left(E_i - E_f + \hbar w_{LO} \right) \tag{4.12}$$

For simplification,k_i is assumed to be zero. Then,

$$Q = k_f \tag{4.13}$$

$$k_f = \left[\frac{2m^*}{\hbar^2}\left(E_i - E_f + \hbar w_{LO}\right)\right]^{\frac{1}{2}} \tag{4.14}$$

In case of LO-phonon emission Equation 4.3 becomes

$$\mathrm{W}i \to f = \frac{m^* e^2 w_{LO}\pi}{\kappa^2 \varepsilon_p}\frac{I^{if}(k_f)}{k_f} \tag{4.15}$$

To obtain the scattering rate due to LO-phonon absorption at non-zero temperature, Equation 4.15 is multiplied by:

$$n = \left[exp\left[\frac{\hbar w_{LO}}{kT}\right] - 1\right]^{-1} \tag{4.16}$$

4.2 Interface Roughness Scattering

During the growth of quantum cascade layers, imperfections cause roughness at the interfaces. Interface roughness introduces scattering centers which leads to the elastic scattering of electrons.

For 1-D case, IFR scattering rate can be expressed as:

$$\frac{1}{\tau_{ij}^{inter,IR}} = \frac{m^*}{\hbar^3}\Lambda^2\Delta^2\sum_m F_m^{ij}\int_0^\pi exp\left(-\frac{q^2(\theta)\Lambda^2}{4}\right)d\theta \tag{4.17}$$

where

$$\widetilde{q} = \sqrt{\frac{2m^* E_{ij}}{\hbar^2}} \tag{4.18}$$

$$E_{ij} = E_i - E_j \tag{4.19}$$

4.3 Radiative Scattering Rate

The radiative scattering rate between two states is expressed as:

$$W_{i,j}^{\text{radiative}} = \frac{e^2 \omega \phi \cos^2(\theta)}{2cn\varepsilon_0} \left|\langle \psi_j(z)|z|\psi_i(z)\rangle\right|^2 \frac{\Gamma}{\left(|E_j - E_i| - \hbar\omega\right)^2 + (\Gamma/2)^2} \quad (4.20)$$

In Equation 4.20, ω is angular frequency of photons, Γ is FWHM of transitions, ϕ is the photon flux and θ represents the angle between electromagnetic radiation and growth direction.

CHAPTER 5

SIMULATION FRAMEWORK

In this chapter, implemented simulation framework is explained in detail. Apart from available open-source simulation tools in the literature, simulation framework is capable of solving quantum cascade laser and quantum cascade detector structures. Simulation framework includes a Schrödinger-Poisson solver, which solves effective-mass Schrödinger-Poisson equation with either transfer matrix approach or finite difference method at conduction band and finds the energy eigenstates with wavefunctions. After finding energy eigenstates and wavefunctions, scattering rates between energy eigenstates are calculated, based on the equations provided in Chapter 4. Simulation framework is based on self-consistent rate equation model as the carrier transport model. In order to find carrier densities in each energy eigenstate, rate equations are solved by a numerical method called 4^{th} order Runge-Kutta method which is implemented within the simulation framework. Also, alternative Runge-Kutta-Fehlberg method is implemented too. Finally, code computes some performance parameters of the device.

5.1 Overview of Simulation Model

Figure 5.1 shows the code structure. The entire code is written in the MATLAB and modules are separate .m files, where each module is responsible for the calculation of specific outputs.

The user defines the input structure by writing the material, material thickness (in nm), the doping density of the layer (in cm^{-3}), applied E-field/bias voltage, applied illumination and temperature in input_file.m script. Materials are located in a .csv

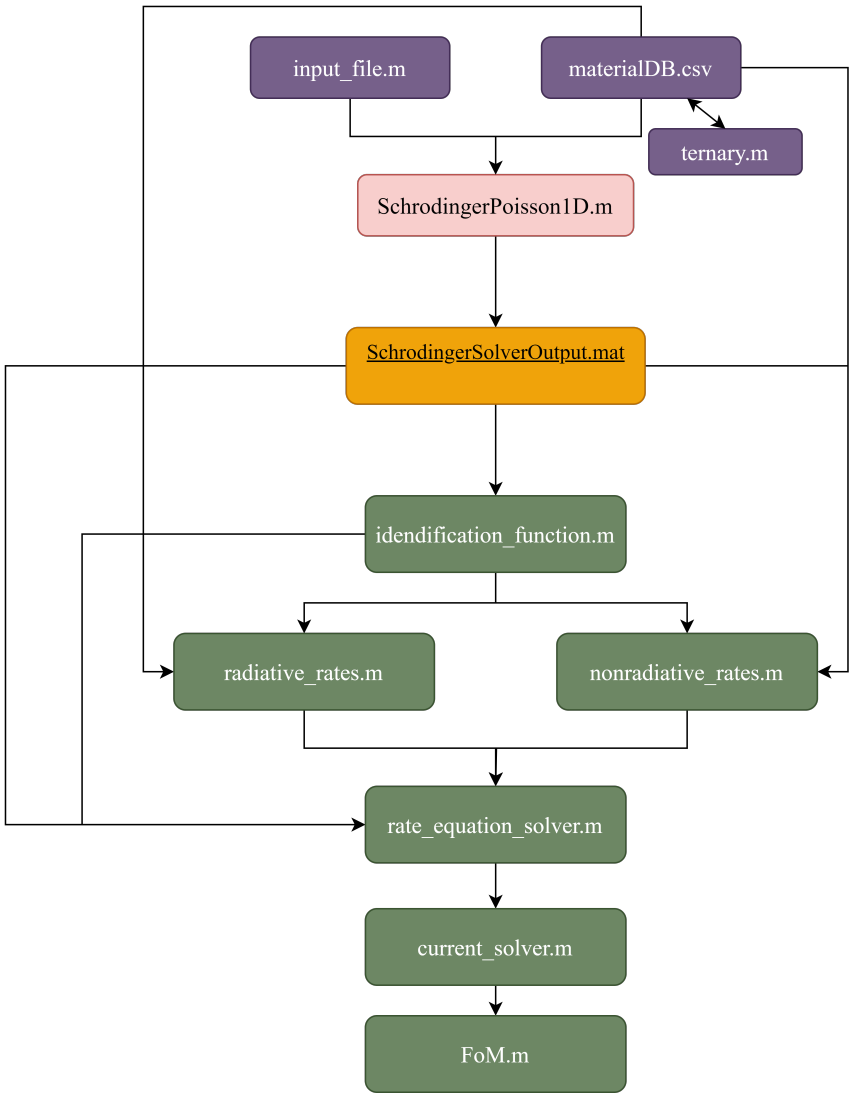

Figure 5.1: Structure of the code

file. To add or modify material parameters, .csv file can be edited. Also, the ternary script allows the construction of ternary alloys with varying mole fractions.

After creating the input file, the "Schrodinger Poisson 1D" script runs. This script solves the self-consistent Schrodinger-Poisson equation, with material parameters taken from the material database. It outputs the wavefunctions and the band diagram data. This step is the most time-consuming part of the simulation. Therefore, to ease the use of the code, the output of the solver is saved as a .mat file named as "Schrodinger Solver Output".

The identification function is the function that determines the wells and barriers in

the input structure and automatically labels the energy eigenstates with their corresponding wavefunctions. Users can modify the labeling for specific purposes in the identification function.

Radiative and non-radiative scattering rates are calculated separately by two different functions: radiative rates function and nonradiative rates function. These functions read the material parameters such as effective mass, LO-phonon energy, etc. from the materials database. For an N-level system, rate functions output NxN matrices of radiative and non-radiative scattering rates. It is possible to activate/deactivate different scattering mechanisms inside the function.

The rate equation solver function computes the steady-state carrier densities in energy sub-bands by solving a system of differential equations with N variables, with 4^{th} order Runge-Kutta method. As an alternative numerical solution, the Runge-Kutta Fehlberg method can be selected in this module.

The current solver function calculates the current through a reference plane. Then, inside the FoM script, some figures of merits and performance parameters are calculated.

5.2 Schrodinger-Poisson Solver

In QCLs and QCDs, carrier transport takes place in the conduction band. Let z axis be the growth direction and x, y are in-plane directions, and consider only the conduction band. This approach called as Ben Daniel-Duke model [32]. Within this approximation, one dimensional Schrodinger equation can be expressed as:

$$\left[-\frac{\hbar^2}{2}\partial_z \frac{1}{m^*(z)}\partial_z + V(z) - E\right]\psi(z) = 0 \tag{5.1}$$

In quantum cascade systems, electrons are not bound since the energy of the eigenstate may exceed the barrier height, especially under the e-field. However, electrons stay in the quantum wells for a substantial time. Therefore, electrons are quasi-bound. Equation 5.1 must be solved numerically for quasi-bound states to obtain energy eigenstates and wavefunctions. The transfer matrix approach and finite difference

method are widely used numerical approaches to solve Equation 5.1.

In the transfer matrix approach, the potential is assumed to be composed of linear and piecewise-constant segments. Then, analytical solutions for each segment are investigated, a transfer matrix relates two successive segments, and using boundary conditions, transfer matrix elements are computed numerically. Then, energy eigenstates and wavefunctions are calculated by using these matrix elements.

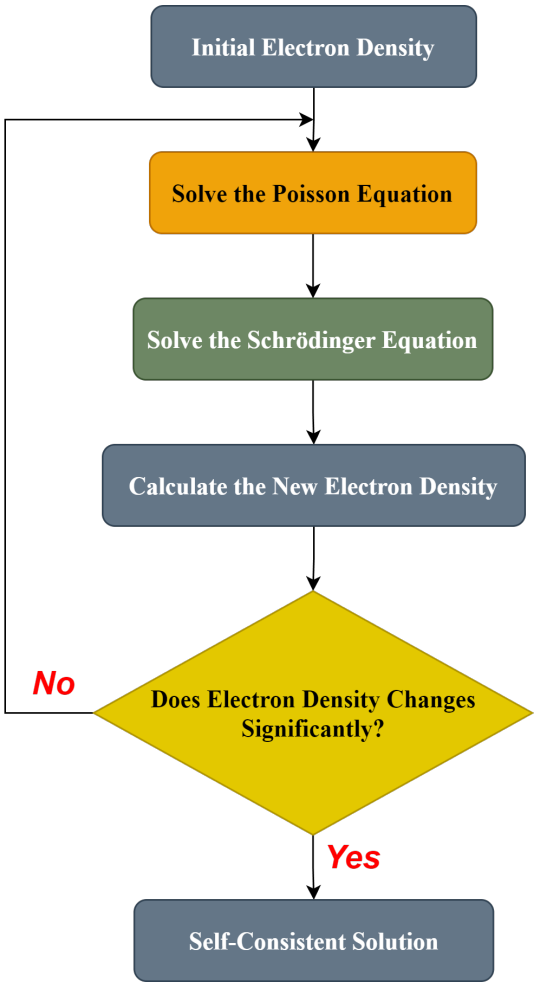

Figure 5.2: Schrodinger-Poisson Solver Flowchart

In the finite difference method, z axis is divided into n equally spaced points with Δ_z grid spacing, and Equation 5.1 is transformed to a finite difference equation. Later, discredited 1-D Schrödinger equation is solved by setting wavefunctions zero at the start and end points of the simulation window.

To include the electrostatic interactions, an additional term from the Poisson equation

is combined with the Schrödinger equation, and the resultant equation is called as Schrödinger-Poisson equation.

The Schrödinger-Poisson solver used in this model is adapted from an open-source work [33]. The flow of the Schrödinger-Poisson solver is given in Figure 5.2 [34].

Schrödinger-Poisson solver module needs an input file that defines the substrate, applied e-field (V/m), temperature (K), and material layers with their thickness (nm) and doping density in the layer (in cm^{-3}). The material database included the following substrates: GaAs, AlAs, InAs, InSb, GaSb, AlSb, InP, GaP, AlP, Si, Ge, and SiGe. Material parameters are located in the database and one can add different materials or edit existing materials by inserting the new material parameters. Default material parameters are taken from [35, 36]. Also, If necessary, the ternary alloy compositions can be arranged inside this module.

Schrödinger-Poisson solver includes two different algorithms: The Finite Difference Method and the Transfer Matrix Method. Either of them can be selected. It is optional to activate the strain model in the code.

Some important parameters which affect the computational time and accuracy are the resolution of the grid, the number of output wavefunctions, and the number of Poisson loops. If non-converging results are obtained, improving the resolution and increasing the number of Poisson loops may give converging results. However, it increases the computation time. After some point, further improving the resolution and increasing the number of loops does not significantly improve the performance of the solver. Therefore, to maintain computational efficiency, the user should find an optimal point for the number of loops and grid resolution.

Schrödinger-Poisson solver provides the following outputs for finding the scattering rates: position-dependent wavefunctions, and conduction band energy. This module is the same for both laser and detector operations.

5.3 Solving Rate Equations to Find State Electron Densities

For calculation of the current in a quantum cascade structure, electron densities in each energy sub-band must be calculated. The rate of change in sub-band i can be expressed as:

$$\frac{dn_i}{dt} = \sum_{j,j\neq i} n_j W_{j,i} - n_i \sum_{j,j\neq i} W_{i,j} \tag{5.2}$$

$W_{i,j}$ is the mean scattering rate, including all optical and non-optical scattering rates from sub-band i to sub-band j. Since quantum cascade structures exhibits translational symmetry, considering two adjacent periods far enough from contacts would be enough for calculations. Let A and B be two adjacent periods and sub-bands in period B represented by superscript +. Due to translational symmetry, Equation 5.2 can be expressed as [37]:

$$\begin{aligned}\frac{dn_i}{dt} = &\sum_{j=1,j\neq i}^{N} n_j W_{j,i} - n_i \sum_{j=1,j\neq i}^{N} W_{i,j} \\ &+ \sum_{j=1,j\neq i}^{N} n_j \left(W_{j,i^+} + W_{j^+,i}\right) - n_i \sum_{j=1,j\neq i}^{N} \left(W_{i^+,j} + W_{i,j^+}\right)\end{aligned} \tag{5.3}$$

For a N-level system, structure is represented as a system of differential equations with N variables which is given in the Equation 5.4

$$Q'(t) = AQ\,(t) \tag{5.4}$$

where $Q(t)$ is the matrix of rates and A is the matrix of coefficients, expressed in Equations 5.5, 5.6

$$Q\,(t) = \begin{bmatrix} n_1(t) \\ n_2(t) \\ ... \\ ... \\ n_N(t) \end{bmatrix} \tag{5.5}$$

$$A = \begin{bmatrix} a_{11} & \cdots & a_{1N} \\ \vdots & \ddots & \vdots \\ a_{N1} & \cdots & a_{NN} \end{bmatrix} \tag{5.6}$$

In the code, "rate equation solver" block forms the A matrix. At that point, a system of differential equations must be solved. For this purpose, two different solvers are implemented in the code: 4$^{\text{th}}$ order Runge-Kutta method and Runge-Kutta-Fehlberg method.

5.3.1 Fourth Order Runge-Kutta Method

The 4$^{\text{th}}$ order Runge-Kutta method (RK-4) is a method to find approximate solutions to differential equations when finding the exact solution is not straightforward. The upgrade mechanism of the method is expressed in the following equations, where $y(t)$ is the function of time with initial value y_0 at time instance of t_0 and h is the step size. Method aims to estimate the slope of the solution at time t.

$$\frac{dy(t)}{dt} = y'(t) = f(y(t),\ t),\ \ y(t_0) = y_0 \tag{5.7}$$

Given the initial conditions, the method estimates the value of exact solution at the next time step by finding intermediate values (or slope at the midpoint between current time step and the next time step), k_1,k_2,k_3,k_4.

$$k_1 = f(y^*(t_0), t_0) \tag{5.8}$$

$$k_2 = f\left(y^*(t_0) + k_1\frac{h}{2}, t_0 + \frac{h}{2}\right) \tag{5.9}$$

$$k_3 = f\left(y^*(t_0) + k_2\frac{h}{2}, t_0 + \frac{h}{2}\right) \tag{5.10}$$

$$k_4 = f(y^*(t_0) + k_3 h, t_0 + h) \tag{5.11}$$

After finding the intermediate values, value of the exact solution at the next time step can be calculated by weighted average of intermediate values as follows:

$$y^*(t_0+h) = y^*(t_0) + \frac{k_1+2k_2+2k_3+k_4}{6}h = y^*(t_0) + mh \tag{5.12}$$

where m represents the weighted average of intermediate values:

$$m = \frac{k_1+2k_2+2k_3+k_4}{6} \tag{5.13}$$

Note that k_2 and k_3 weigh more than k_1 and k_4 since they yield a better estimate. Steps are repeated until until the time interval is covered.

Considering Equations 5.5, 5.6, 4$^{\text{th}}$ Order Runge-Kutta method becomes

$$k_1 = AQ^*(t_0) \tag{5.14}$$

$$k_2 = A\left(Q^*(t_0) + k_1\frac{h}{2}\right) \tag{5.15}$$

$$k_3 = A\left(Q^*(t_0) + k_2\frac{h}{2}\right) \tag{5.16}$$

$$k_4 = A\left(Q^*(t_0) + k_3 h\right) \tag{5.17}$$

$$Q^*(t_0+h) = Q^*(t_0) + \frac{k_1+2k_2+2k_3+k_4}{6}h = Q^*(t_0) + mh \tag{5.18}$$

for

$$m = \frac{k_1+2k_2+2k_3+k_4}{6} \tag{5.19}$$

In summary, associated rate equations for different energy levels is solved by this method.

5.3.2 Runge-Kutta-Fehlberg Method

As an alternative to the 4th order Runge-Kutta method, Runge-Kutta-Fehlberg (RKF) method is implemented too. The RKF method is particularly useful when the desired accuracy of the solution is not known.

$$\frac{dy(t)}{dt} = y'(t) = f(y(t), t), \quad y(t_0) = y_0 \tag{5.20}$$

Similar to RK-4 method, k_1,k_2,k_3,k_4,k_5,k_6 are sets of intermediate values to be calculated.

$$k_1 = f(y^*(t_0), t_0) \tag{5.21}$$

$$k_2 = f(y^*(t_0) + k_1\frac{h}{4}, t_0 + \frac{h}{4}) \tag{5.22}$$

$$k_3 = f(y^*(t_0) + k_1\frac{3h}{32} + k_2\frac{9h}{32}, t_0 + \frac{3h}{8}) \tag{5.23}$$

$$k_4 = f(y^*(t_0) + k_1\frac{1932h}{2197} - k_2\frac{7200h}{2197} + k_3\frac{7296h}{2197}, t_0 + \frac{12h}{13}) \tag{5.24}$$

$$k_5 = f(y^*(t_0) + k_1\frac{439h}{216} - k_2 8h + k_3\frac{3680h}{513} - k_4\frac{845h}{4104}, t_0 + h) \tag{5.25}$$

$$k_6 = f(y^*(t_0) - k_1\frac{8h}{27} + k_2 2h - k_3\frac{3544h}{2565} + k_4\frac{1859h}{4104} - k_5\frac{11h}{40}, t_0 + \frac{h}{2}) \tag{5.26}$$

5th order estimate is expressed as:

$$y^*_{5th}(t_0 + h) = y^*(t_0) + k_1\frac{25h}{216} + k_3\frac{1408h}{2565} + k_4\frac{2197h}{4104} - k_5\frac{h}{5}, \tag{5.27}$$

Where 4th order estimate is expressed as:

$$y^{*}_{4th}(t_0+h) = y^{*}(t_0) + k_1\frac{16h}{135} + k_3\frac{6656h}{12825} + k_4\frac{28561h}{56430} - k_5\frac{9h}{50} + k_6\frac{2h}{55}, \quad (5.28)$$

difference between the 4th and 5th order estimates to estimate error:

$$e(t+h) = |y^{*}_{5th}(t_0+h) - y^{*}_{4th}(t_0+h)|, \quad (5.29)$$

Based on the estimated error, the method adjusts the step size h to maintain the desired accuracy. Step size can be increased for efficiency, if the error is within a tolerance limit. If the error exceeds the tolerance, the step size is decreased to improve accuracy. Calculations are repeated until until the time interval is covered.

5.4 Calculation of the Current

After finding the carrier densities in each sub-band, current is calculated by "current solver" block, through a reference plane between two adjacent periods as:

$$J_{total} = e\sum_{i\in A, j\in B}(n_i W_{i,j} - n_j W_{j,i}) \quad (5.30)$$

For detector operation, if optical term of transition rates is switched off, dark current density of the photodetector can be calculated:

$$J_{dark} = e\sum_{i\in A, j\in B}(n_i W_{i,j,non-optical} - n_j W_{j,i,non-optical}) \quad (5.31)$$

Photocurrent can be calculated by using Equations 5.30, 5.32:

$$J_{photo} = J_{total} - J_{dark} \quad (5.32)$$

CHAPTER 6

SIMULATION OUTPUTS

In this chapter, outputs of proposed simulation tool are presented for different structures such as evaluation of LO-phonon scattering lifetime in a single well, calculation of sub-band populations and gain in a quantum cascade laser and investigation of photocurrent and responsivity of a quantum cascade detector.

6.1 Evaluation of LO-phonon scattering lifetime in a single quantum well

In this section, the LO-phonon scattering lifetime in a single quantum well is calculated and results are compared with the results in [38] to verify the simulation framework. The barrier material is $Al_{0.3}Ga_{0.7}As$ and the well material is $GaAs$. Conduction band energy diagram and wavefunctions for the quantum well thickness of $12\,\mathrm{nm}$ is illustrated in Figure 6.1

To obtain similar results, the material database is updated w.r.t. parameters given in Table 8.1 [38].

Table 6.1: Material Parameters for Simulation

Material Parameter for Simulation	**Value**
Electron Effective Mass for GaAs (m_e)	0.007 m_0
Static Dielectric Constant for GaAs (ϵ_s)	12.5
LO-phonon energy for GaAs	36 meV
Conduction Band Offset	214 meV

The thickness of the $GaAs$ quantum well is changed from 3 nm to 18 nm and the

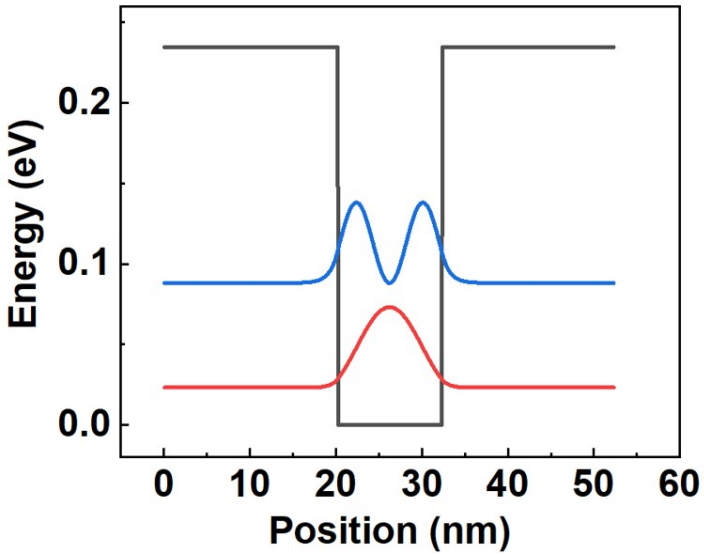

Figure 6.1: $GaAs/Al_{0.3}Ga_{0.7}As$ Quantum Well with 12nm thickness

LO-phonon scattering lifetime from 2nd state to 1st is calculated. Simulation results are given in Figure 6.2. Calculated results are close to the presented result in the reference [38].

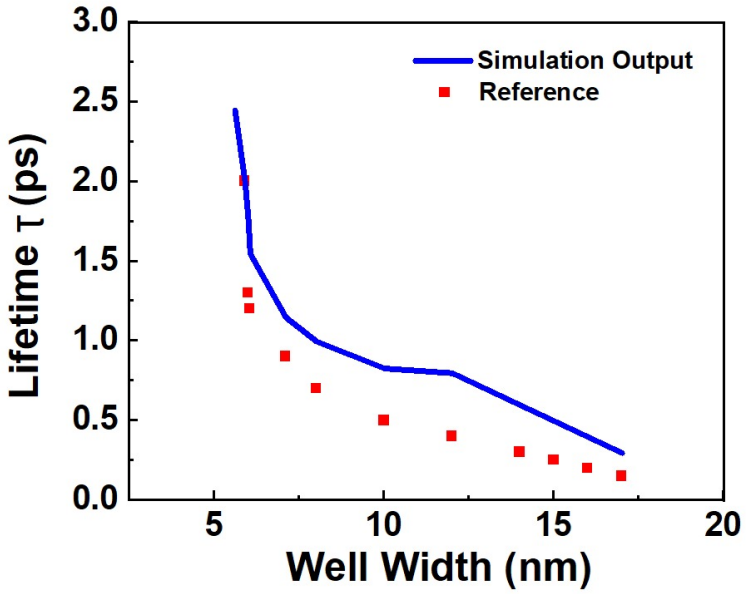

Figure 6.2: $GaAs/Al_{0.3}Ga_{0.7}As$ LO-Phonon lifetime with varying QW thickness

6.2 Simulation of a Quantum Cascade Laser

In this section, a $GaAs/Al_{0.33}Ga_{0.67}As$ quantum cascade laser presented in [39] is simulated. Layer thicknesses (in nm), starting from $Al_{0.33}Ga_{0.67}As$ barrier, for 1 period of the structure are given as follows:

4/3.2/2/2.8/2.3/2.3/2.5/2.3/2.5/2.1/5.8/1.5/2/4.9/1.7/4/3.4.

Laser transition occurs in GaAs QW with 4.9 nm width. The actual device consists of 40 periods but in this simulation, 1.5 periods of the device is investigated. Figure 6.3 shows the 1.5 periods of the gain medium with injectors.

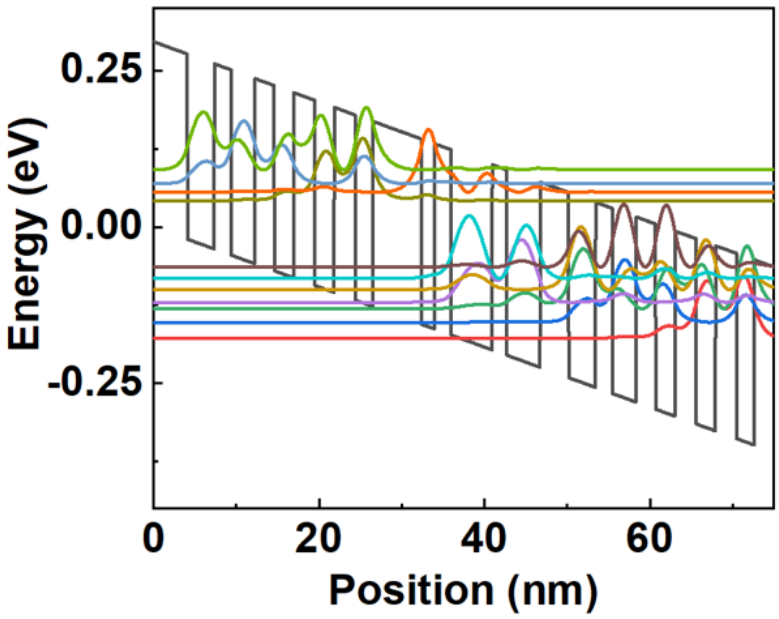

Figure 6.3: $GaAs/Al_{0.33}Ga_{0.67}As$ QCL from [39]

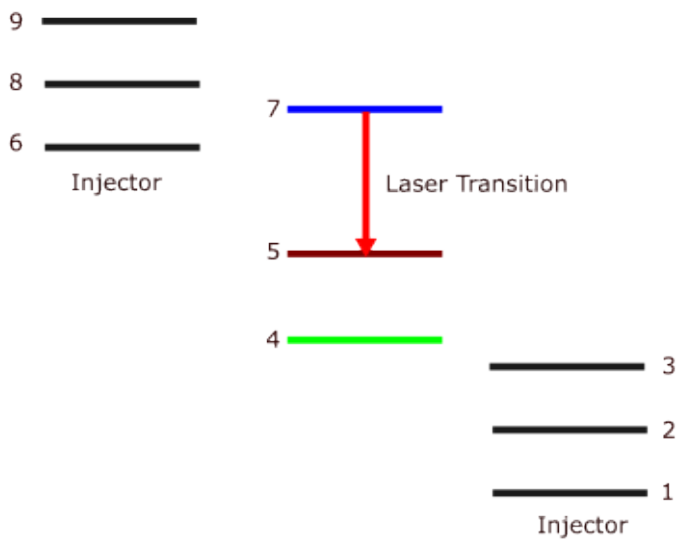

Figure 6.4: Nine-level system and transitions,redrawn after [39]

Energy eigenstates are labeled as shown in Figure 6.4. In nine level system, laser transition occurs between states 7 and 4. As stated in the reference [39], upward transitions from states 1,2,3 to state 7 is ignored. Also, states 1,2,3 and 6,8,9 are assumed isolated.

After the calculation of scattering rates, rate equations are solved. Steady-state carrier densities are shown in Figure 6.5. Results are similar to the results presented in [39].

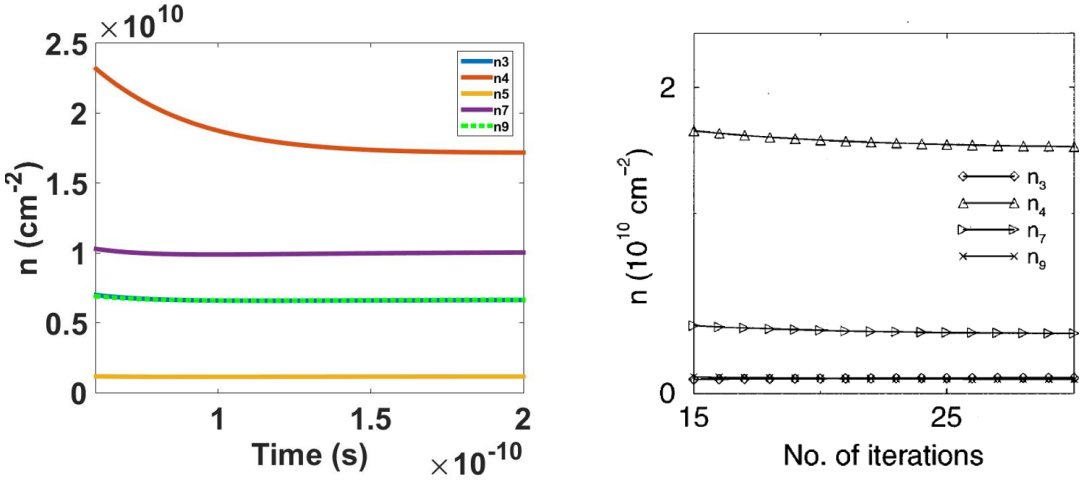

(a) (b)

Figure 6.5: Solution of differential equations for sub-band populations,(a) Simulation results and (b) reference [39]

After finding sub-band populations, the gain of the laser is calculated w.r.t. Equation 6.1. For gain calculation, values in Table 6.2 are taken from the reference.

$$g = \frac{4\pi q}{\epsilon_0 n} \frac{(\tau_{75} - \tau_5)(\tau_7/\tau_{75})}{2\gamma_{75} L_p} \frac{(z_{75})^2}{\lambda} \tag{6.1}$$

Table 6.2: Material Parameters for Simulation

Material Parameter for Simulation	**Value**
n	3.2836
γ_{75}	5.5 meV
O_{75}	0.635 $m^{-1}s^2$

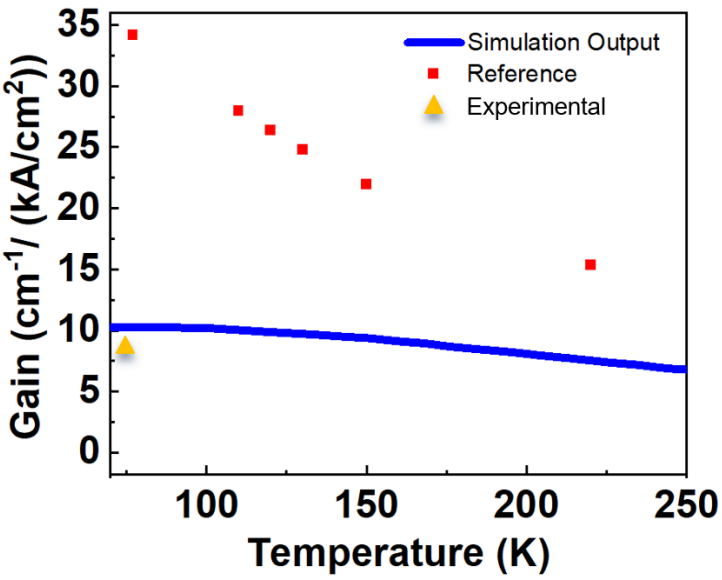

Figure 6.6: Gain of the laser for different temperatures

Gain decreases with increasing temperature, since at low temperature values, the non-radiative scattering rate of the excited level of the laser is low and it increases with increasing temperature.

Experimentally measured gain at T=77K was reported as 8.7 $cm^{-1}/(kA/cm^{-2})$ and the calculated gain at T=77 K is found 10.28 $cm^{-1}/(kA/cm^{-2})$.

6.3 Simulation of InGaAs/InAlAs Quantum Cascade Detector

In this section, the QCD presented in [28] as N1020 is simulated. QCD consists of alternating $In_{0.52}Ga_{0.48}As/In_{0.53}Al_{0.47}As$ layers. The layer sequence (in nm) is as follows: 5/4.05/4.7/4.8/4.5/6.2/4.1/10.7. 10.7 nm layer corresponds to a QW where radiative excitation occurs and it is doped with $2x10^{17}cm^{-3}$ doping density. Other layers do not contain any intentional doping. Figure 6.7 shows the three periods of the device and calculated wavefunctions.

Figure 6.8 represents the structure with 5 energy levels. Photon absorption excites electrons at State 1 to State 5. State 1 and State 5 can be called active region states. Absorbed electrons are scattered/transferred to the next active region through extractor states 4,3,2. Carrier dynamics are also affected by the next neighbor period's

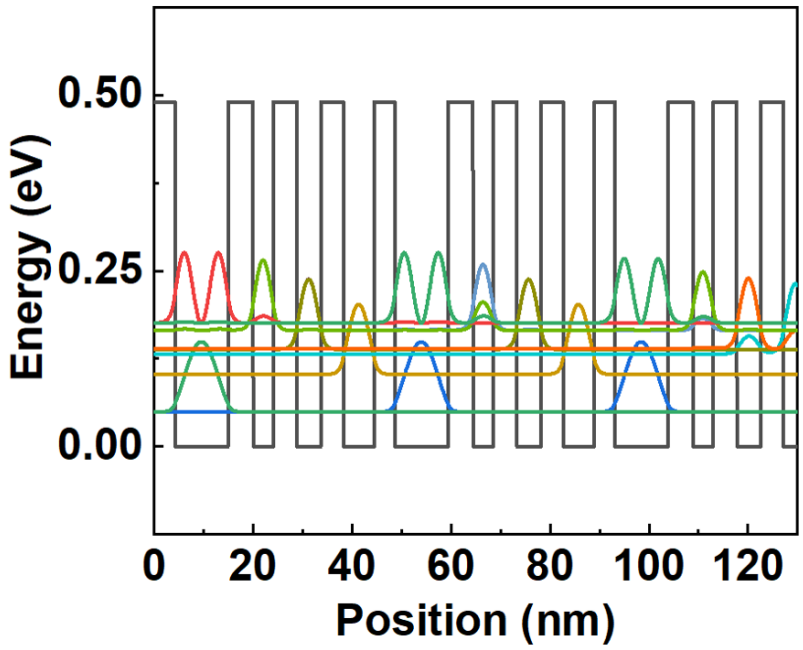

Figure 6.7: $In_{0.52}Ga_{0.48}As/In_{0.53}Al_{0.47}As$ QCD from [28]

states, they are represented by superscript +.

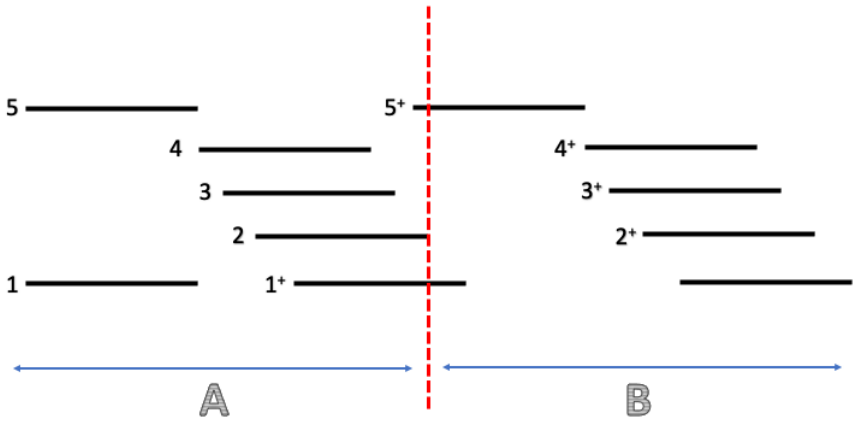

Figure 6.8: Five level representation of the structure

The current density of the illuminated structure is calculated through a reference plane, drawn with the red line in Figure 6.8. Photocurrent density is calculated as:

$$J_{photo} = e \sum_{i \in A, j \in B} \left(\frac{n_i}{\tau_{ij}} - \frac{n_j}{\tau_{ji}} \right) \tag{6.2}$$

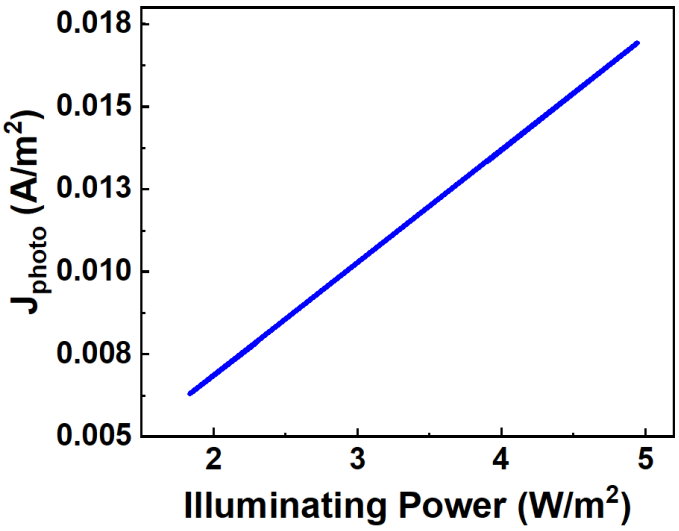

Figure 6.9: Photocurrent of QCD for under varying illuminating power density

Figure 6.9 shows the photocurrent density for varying illuminating power density.

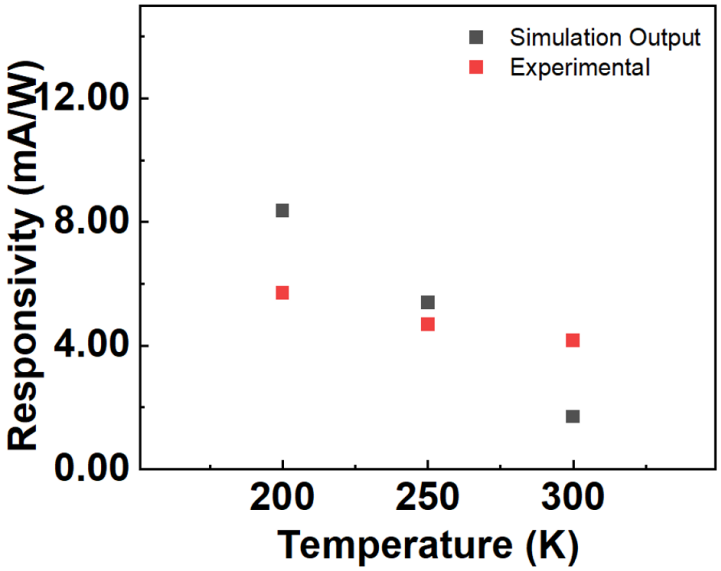

Figure 6.10: Responsivity of QCD for different temperature values

The responsivity of the detector is defined as follows:

$$R = \left(\frac{J_{\text{photo}}}{P_{\text{in}}} \right) \tag{6.3}$$

In Figure 6.10, photocurrent at $10\,\mathrm{W\,m^{-2}}$ illuminating power density for varying

temperatures is calculated and responsivity of the QCD is calculated.

CHAPTER 7

DESIGN OF BI-FUNCTIONAL QCLD FOR 3-4 μm

In this chapter, a bi-functional quantum cascade laser/detector design for in $3-4\,\mu\mathrm{m}$ window is presented and design considerations such as choosing an appropriate material system, active well design, injector design, and wavelength matching is explained. Design is conducted on a commercial software. Apart from conventional QCL and QCD designs, proposed structure has some unique aspects. Wavelength matching allows for efficient coupling between the emitted and detected light, maximizing the device's overall performance. This characteristic is crucial for applications that require accurate and reliable sensing in the $3-4\,\mu\mathrm{m}$ spectral range. Also, thanks to bi-functional design, two functionalities integrated in a single unit which simplifies the design steps and reduces the overall complexity. While designing the bi-functional QCLD, trade-offs between laser performance and detector performance is managed to obtain a device without degraded performance.

7.1 Selection of Material System

As explained in previous chapters, in devices that utilize interband transitions, the energy band gap determines the range of operation wavelength. However, in quantum cascade devices which based on intersubband transitions, conduction band discontinuity (ΔE_C) determines the range of operation wavelength.

Commonly used $In_{0.53}Ga_{0.47}As/In_{0.52}Al_{0.48}As$ material system lattice matched to InP substrate has $\Delta E_C = 527meV$ which allows maximum radiative transitions at $290\,\mathrm{meV}$ which corresponds to $4.275\,\mu\mathrm{m}$. Therefore, for obtaining a shorter wavelength to operate in $3-4\,\mu\mathrm{m}$ window, a material system with larger ΔE_C is needed.

$In_{0.7}Ga_{0.3}As/In_{0.4}Al_{0.6}As$ material system lattice matched to InP substrate offers $\Delta E_C = 791meV$ is suitable for operation in the desired wavelength range. Figure 7.1 shows the conduction band energy diagram for $In_{0.4}Al_{0.6}As$ quantum well with 10 Å thickness, in between 10 Å thick $In_{0.7}Ga_{0.3}As$ barriers.

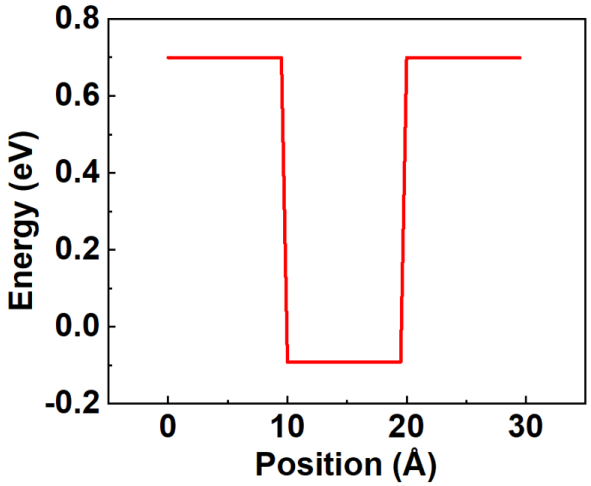

Figure 7.1: Conduction band energy diagram for $In_{0.7}Ga_{0.3}As/In_{0.4}Al_{0.6}As$ material system

7.2 Active Region Design

While designing the active region, laser operation is considered first. Later, the designed QCL will be engineered for QCD operation.

For the two-quantum well given in Figure 7.2, the radiative transition occurs in states localized in the same quantum well. This type of transition is called vertical transition. The ground state of the quantum well is in resonance with the following quantum well's ground state, generally so that extraction is provided by resonant tunneling. Utilizing vertical transitions have some advantages. Since upper and lower state wavefunctions are spatially overlaps, the optical matrix element is high, which is an indicator of strong interaction between states.

Figure 7.2 shows the designed two-quantum well active region, under e-field of $92\,\mathrm{kV\,cm^{-1}}$. The radiative transition occurs between state 3 and state 2. State 1 is the extraction level. At T= 77 K, the energy difference between state 3 and state 2

is equal to $371\,\mathrm{meV}$. State 2 and state 1 are separated by $32.6\,\mathrm{meV}$, which is close to the LO-phonon energy of the material ($37.7\,\mathrm{meV}$), to effectively de-populate state 2 with LO-phonon scattering.

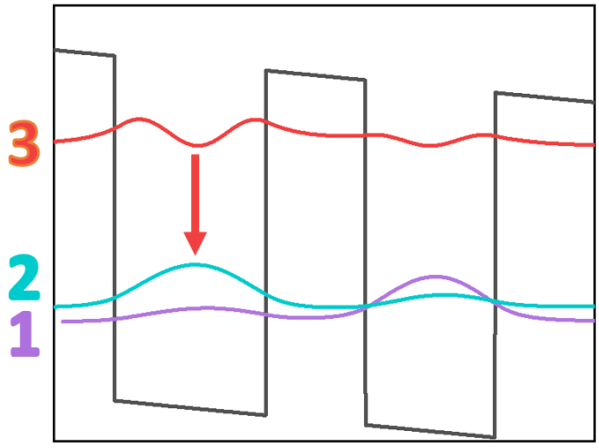

Figure 7.2: Two-well active region of the laser

Table 7.1 gives the upper and lower laser level lifetime, the energy difference between the upper and lower laser, and the figure of merit (FoM) for three different temperatures. The figure of merit is defined as:

$$FoM = \tau_3 \left(1 - \frac{\tau_3}{\tau_2}\right) z_{32} \tag{7.1}$$

The figure of merit value can be perceived as a measure of population inversion combined with an optical dipole matrix element between selected states (a measure of optical transition between states). Therefore, a high figure of merit indicates a higher lasing probability between selected states.

7.3 Injector Design

Injector states are separated by LO-phonon energy, to reach the most efficient carrier scattering due to LO-phonon scattering through a miniband. A funnel-type injector includes a minigap that prevents electron escape onto the continuum or states in the other valleys.

Table 7.1: Simulation outputs for different temperatures

Temperature (K)	$\tau_3(ps)$	$\tau_2(ps)$	$E_3 - E_2(meV)$	FoM
77	3.19	0.38	371	355
150	3.29	0.39	369.9	379
300	3.94	0.44	367.5	421

7.4 Overall Design for Laser

By integrating the active region and injector, the structure given in Figure 7.3 is obtained. Figure 7.3 shows the conduction band diagram of given structure and energy levels with related squared-wave functions. Starting from the injector barrier, layer thickness (in angstrom) of a single period of the device is as follows:

45/35/23/30/28/20/18/18/18/19/18/15/20/15/23/14/25/13/30/13/34/12/36/11.

Underlined wells are injector wells and doped with Si where doping density is $2.5 \times 10^{17}\,\mathrm{cm}^{-3}$

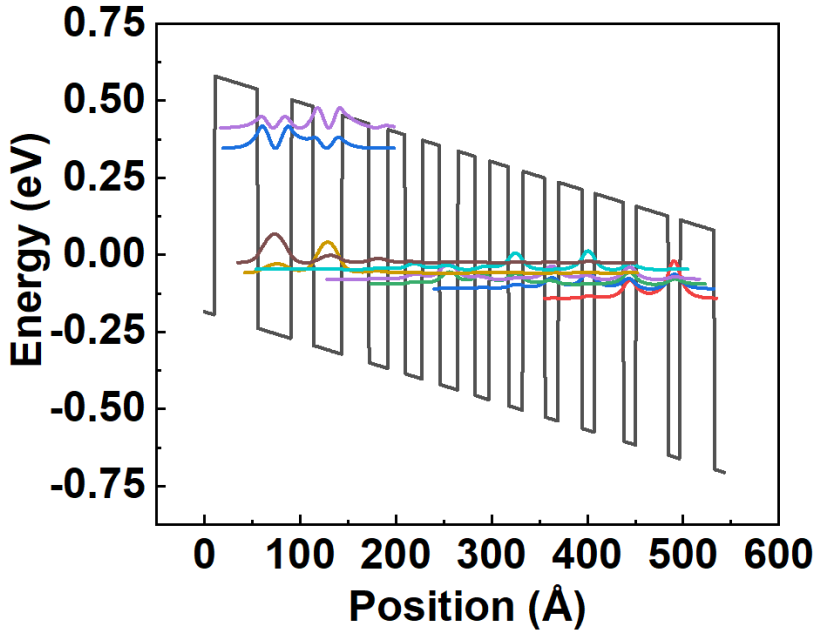

Figure 7.3: 1 period of designed QCL

7.5 Investigation of Designed Structure for Photodetection

After designing the QCL, which operates at $3.37\,\mu\mathrm{m}$ (at $300\,\mathrm{K}$) under e-field of $92\,\mathrm{kV\,cm^{-1}}$, the structure will be investigated under zero bias. Figure 7.4 shows the 1 period of the structure under zero E-field.

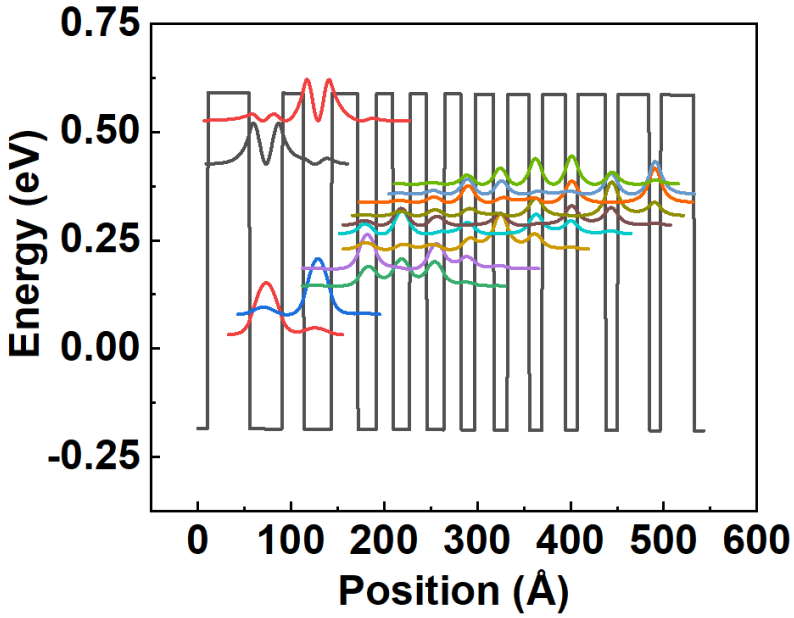

Figure 7.4: 1 period of the device, zero E-field

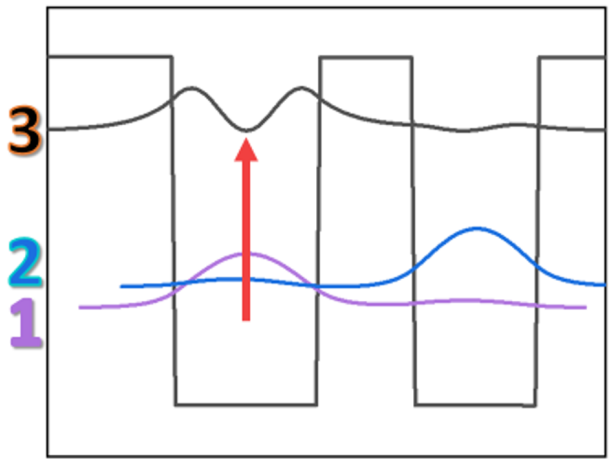

Figure 7.5: Two well active region of the detector

In thermodynamic equilibrium, assuming no incident radiation, most of the electrons are in the extractor level of the first well of the active region (state 1). Therefore, the

optical transition of the detector occurs between the extraction level and the upper laser level, which is illustrated in Figure 7.5. This means, there exists an intrinsic wavelength shift between lasing wavelength and the detection wavelength. For the proposed structure, state 3 and state 1 energy difference is calculated as $394\,\mathrm{meV}$ (at $300\,\mathrm{K}$), which corresponds to at $3.14\,\mu\mathrm{m}$. The detector is blue-shifted with respect to the laser.

7.6 Wavelength Matching for QCL and QCD

In this design, matching the lasing and detection wavelengths will be aimed without compromising laser performance and improving detector performance at room temperature.

Wavelength matching can be achieved by inserting a thin well and a thin barrier between the injector and active quantum well [40]. A thin well is designed such that its energy levels are coupled to the active well and degenerates the energy level 3 and energy level 2 of the active well. In this way, energy shift is compensated. The amount of compensation provided by a thin well depends on the width of the thin well.

Figure 7.6 shows the difference between laser and detector transition energies, and the detector state's dipole matrix element with respect to increasing width of thin well, where thin barrier width equal to $10\,\text{Å}$.

Also Figure 7.7 shows the amount of shift and laser state's dipole matrix element with respect to increasing width of the thin well.

Further increasing the well width makes optical transitions more diagonal, rather than vertical. This reduces the both laser and detector dipole, thus degrading the performance. The optimal thickness for energy compensation without degrading bifunctional operation is found as 7 Å. The final layer thickness (in Å) of one period of the device is as follows:

40/7/10/38/19/33/30/22/20/20/20/<u>20</u>/20/<u>17</u>/22/<u>15</u>/25/<u>13</u>/27/15/33/15/35/11/37/12.

Underlined wells are injector wells and doped with Si where doping density is $2.5\times$

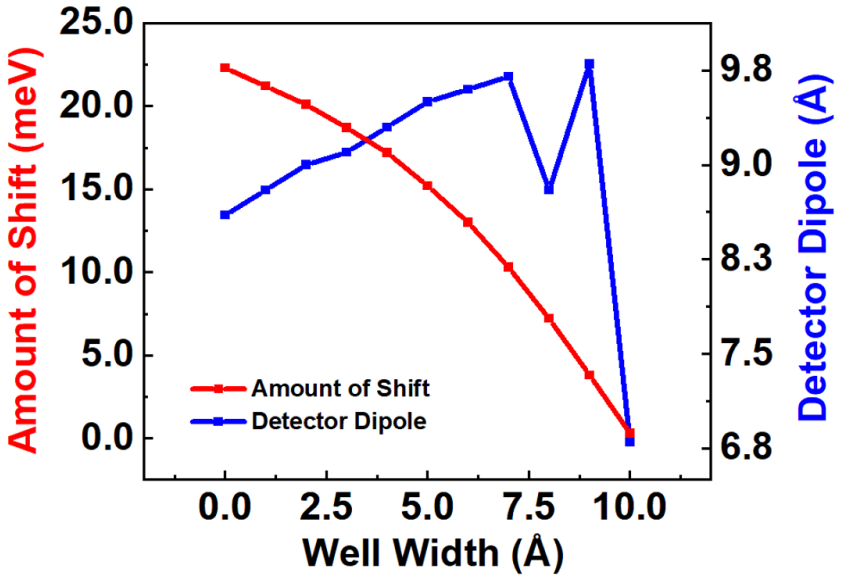

Figure 7.6: Energy shift and detector's dipole for varying thin layer thickness

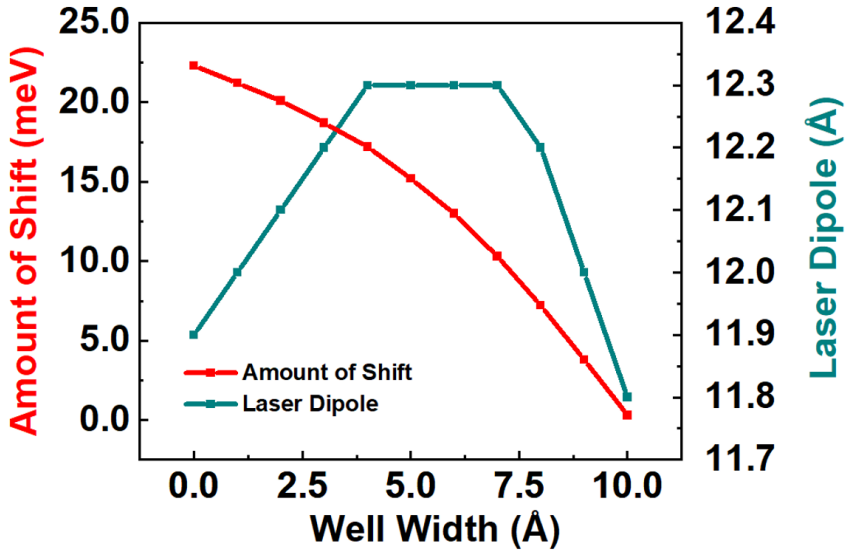

Figure 7.7: Energy shift and laser's dipole for varying thin layer thickness

$10^{17}\,\mathrm{cm}^{-3}$.

Table 7.2 shows the upper and lower laser level lifetime, the energy difference between upper and lower laser and figure of merit (FoM) of shift compensated QCLD for 300 K.

Figure 7.8 shows the one-period conduction band diagram of shift compensated

Table 7.2: Simulation outputs for shift compensated design at T=300 K, for laser operation

Temperature (K)	$\tau_3(ps)$	$\tau_2(ps)$	$E_3 - E_2(meV)$	FoM
300	2.78	0.35	355.6	456

structure and energy levels with related squared-wave functions, under e-field of $92\,\mathrm{kV\,cm^{-1}}$, which corresponds to laser operation.

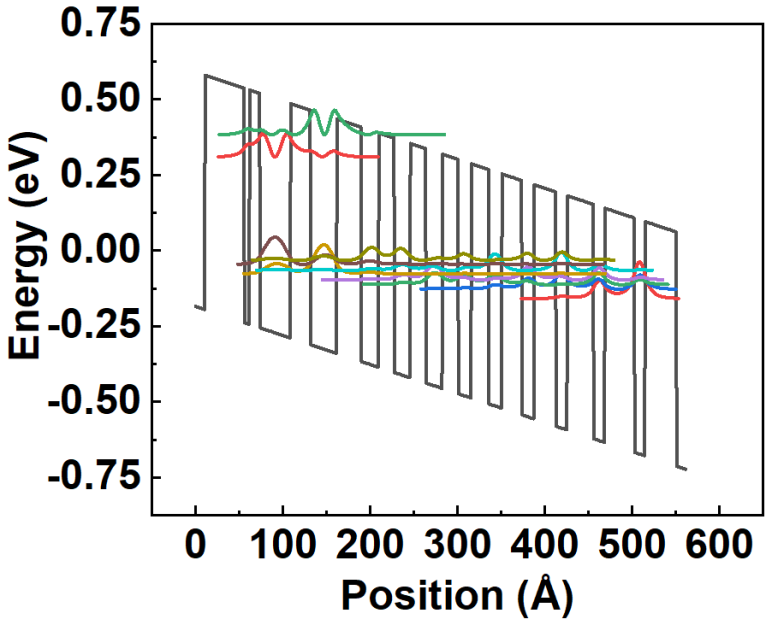

Figure 7.8: Conduction band diagram of one period of shift compensated device, under e-field

Figure 7.9 shows the one period conduction band diagram of shift compensated structure and energy levels with related squared-wave functions, under zero bias, which corresponds to detector operation.

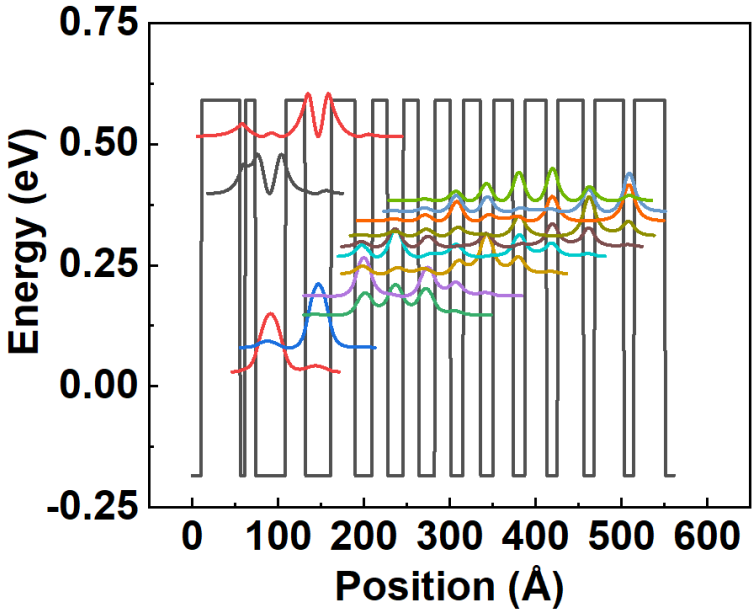

Figure 7.9: Conduction band diagram of one period of shift compensated device, under zero bias

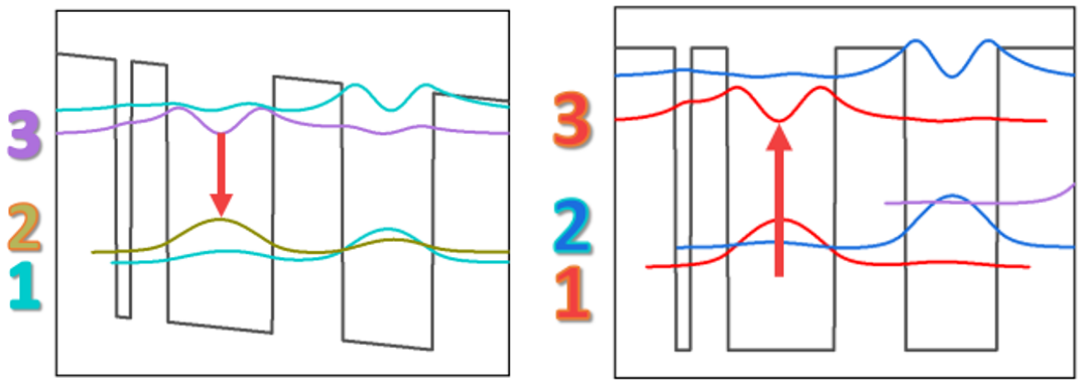

(a) (b)

Figure 7.10: Three well active region, after the insertion of thin well and thin barrier

Figure 7.10 gives a closer look to the active well and energy states in the active well, after the insertion of 7 Å thin well and 10 Å thin barrier.

In conclusion, before inserting a thin well and barrier between the injector and active well, QCL was operating at 3.37 µm where QCD at 3.14 µm. After insertion of the thin well and barrier, QCL operates at 3.51 µm, and QCD operates at 3.41 µm. FoM

for laser is increased slightly from $421\,\mathrm{ps\,\mathring{A}^2}$ to $456\,\mathrm{ps\,\mathring{A}^2}$ and detector dipole is increased from $8.6\,\mathring{\mathrm{A}}$ to $9.7\,\mathring{\mathrm{A}}$. All in all, wavelength shift is reduced without degrading the device's performance.

CHAPTER 8

CONCLUSION AND FUTURE WORK

Bi-functional quantum cascade structures are good candidates as transmitters and receivers in photonic integrated circuits. The idea of using the same epilayer for enabling monolithic integration for on-chip applications can be realized by bi-functional QCLDs.

In this work, a simulation tool coded on MATLAB for modeling bi-functional quantum cascade devices such as QCLs and QCDs, based self-consistent rate equation model is provided. The whole code is published on GitHub as open-source. Starting from simple test cases (like single quantum well) to more complex structures (like QCL and QCD), simulation results show good agreement with the experimental results provided by the literature and other available simulation tools. With the capabilities of the provided simulation tool, the active region of a bi-functional device can be designed. However, simulation tool's output deviates from expected results for extreme high and extreme low temperatures. This problem can be solved by implementing a new Schrodinger-Poisson solver not only relies on effective mass approximation and includes other methods such as 6x6 or 8x8 k.p approximations, which can be a topic of another Ph.D. study. Also,to reduce the computational time, code can be programmed in other programming languages such as C or Python in a structured manner.

Also, in this work, a unique QCLD structure is designed with proposed simulation tool and aid of commercial software. The designed structure offers reduced intrinsic wavelength shift between QCL and QCD operations, without compromising device performance.

However, only designing the active region of QCLDs is not enough to fabricate a real device. For further studies, in addition to active region design, with waveguide design and thermal modeling of the device, a complete device can be designed for fabrication. After epitaxial growth and packaging, a device can be fabricated and characterized. Also, this work can complement and be integrated with former works on on-chip applications [41, 42, 43, 44], infrared photodetectors [45, 46, 47, 48, 49], optical modulators [50, 51, 52, 53, 54] as well as linear optical quantum computing [55, 56], conducted by our research group.

REFERENCES

[1] R. F. Kazarinov, "Possibility of amplication of electromagnetic waves in a semiconductor with a superlattice," *Sov. Phys. Semicond.*, vol. 5, no. 4, pp. 707–709, 1971.

[2] J. Faist, F. Capasso, D. L. Sivco, C. Sirtori, A. L. Hutchinson, and A. Y. Cho, "Quantum cascade laser," *Science*, vol. 264, no. 5158, pp. 553–556, 1994.

[3] D. Hofstetter, M. Beck, and J. Faist, "Quantum-cascade-laser structures as photodetectors," *Applied Physics Letters*, vol. 81, pp. 2683–2685, 10 2002.

[4] C. Jirauschek, J. Popp, M. Haider, M. Franckié, and J. Faist, "Ensemble Monte Carlo modeling of quantum cascade detectors," *Journal of Applied Physics*, vol. 130, p. 203103, 11 2021.

[5] J. Faist, *Quantum Cascade Lasers*. Oxford University Press, 03 2013.

[6] C. Sirtori, F. Capasso, J. Faist, A. L. Hutchinson, D. L. Sivco, and A. Y. Cho, "Resonant tunneling in quantum cascade lasers," *IEEE journal of quantum electronics*, vol. 34, no. 9, pp. 1722–1729, 1998.

[7] B. Bozok, *Mid-infrared quantum cascade laser*. PhD thesis, Bilkent Universitesi (Turkey), 2017.

[8] H. Page, A. Robertson, C. Sirtori, C. Becker, G. Glastre, and J. Nagle, "Gaas quantum cascade lasers (/spl lambda/ /spl ap/ 11.5 /spl mu/m) operating on a peltier element with laser action up to 15/spl deg/c," in *Technical Digest. Summaries of papers presented at the Conference on Lasers and Electro-Optics. Postconference Technical Digest (IEEE Cat. No.01CH37170)*, pp. 325–326, 2001.

[9] H. Page, C. Becker, A. Robertson, G. Glastre, V. Ortiz, and C. Sirtori, "300 K operation of a GaAs-based quantum-cascade laser at $\lambda \approx 9$ μm," *Applied Physics Letters*, vol. 78, pp. 3529–3531, 05 2001.

[10] J. Faist, C. Sirtori, F. Capasso, D. L. Sivco, J. N. Baillargeon, A. L. Hutchinson, and A. Y. Cho, "High-power long-wavelength (/spl lambda//spl sim/11.5 μm) quantum cascade lasers operating above room temperature," *IEEE Photonics Technology Letters*, vol. 10, no. 8, pp. 1100–1102, 1998.

[11] J. Faist, M. Beck, T. Aellen, and E. Gini, "Quantum-cascade lasers based on a bound-to-continuum transition," *Applied Physics Letters*, vol. 78, no. 2, pp. 147–149, 2001.

[12] A. Wittmann, M. Giovannini, J. Faist, L. Hvozdara, S. Blaser, D. Hofstetter, and E. Gini, "Room temperature, continuous wave operation of distributed feedback quantum cascade lasers with widely spaced operation frequencies," *Applied physics letters*, vol. 89, no. 14, p. 141116, 2006.

[13] J. Faist, F. Capasso, C. Sirtori, D. L. Sivco, J. N. Baillargeon, A. L. Hutchinson, S.-N. G. Chu, and A. Y. Cho, "High power mid-infrared ($\lambda \sim 5\mu$m) quantum cascade lasers operating above room temperature," *Applied Physics Letters*, vol. 68, no. 26, pp. 3680–3682, 1996.

[14] J. Yu, S. Slivken, A. Evans, and M. Razeghi, "High-performance, continuous-wave quantum-cascade lasers operating up to 85° c at $\lambda \sim 8.8\mu$m," *Applied Physics A*, vol. 93, pp. 405–408, 2008.

[15] J. Faist, F. Capasso, D. L. Sivco, A. L. Hutchinson, S.-N. G. Chu, and A. Y. Cho, "Short wavelength ($\lambda \sim 3.4\ \mu m$) quantum cascade laser based on strained compensated ingaas\alinas," *Applied Physics Letters*, vol. 72, no. 6, pp. 680–682, 1998.

[16] M. P. Semtsiv, S. Dressler, and W. T. Masselink, "Short-wavelength ($\lambda \approx 3.6\ \mu$m) $in_{0.73}ga_{0.27}as$–alas–inp quantum-cascade laser," *IEEE Journal of Quantum Electronics*, vol. 43, no. 1, pp. 42–46, 2007.

[17] J. Commin, D. Revin, S. Zhang, A. Krysa, K. Kennedy, and J. Cockburn, "High peak power $\lambda \sim 3.3$ and $3.5\ \mu m$ ingaas/alas(sb) quantum cascade lasers operating up to 400 k," *Applied Physics Letters*, vol. 97, no. 3, p. 031108, 2010.

[18] I. P. Marko, A. R. Adams, S. J. Sweeney, R. Teissier, A. N. Baranov, and S. Tomić, "Evidence of carrier leakage into the l-valley in inas-based quan-

tum cascade lasers under high hydrostatic pressure," *Physica Status Solidi (b)*, vol. 246, no. 3, pp. 512–515, 2009.

[19] A. Delga, *Quantum cascade detectors: A review*. Elsevier, 1 2019.

[20] A. Mirčetić, D. Indjin, V. Milanović, P. Harrison, Z. Ikonić, R. Kelsall, M. Giehler, R. Hey, and H. Grahn, "Gaas/algaas quantum cascade lasers based on double resonant electron–lo phonon transitions," in *Materials Science Forum*, vol. 494, pp. 25–30, Trans Tech Publ, 2005.

[21] R. C. Iotti and F. Rossi, "Microscopic theory of semiconductor-based optoelectronic devices," *Reports on Progress in Physics*, vol. 68, no. 11, p. 2533, 2005.

[22] L. C. West, "Spectroscopy of gaas quantum wells," 7 1985.

[23] M. Moradinasab, *Optical properties of semiconductor nanostructures*. PhD thesis, 2015.

[24] F. R. Giorgetta, E. Baumann, M. Graf, Q. Yang, C. Manz, K. Kohler, H. E. Beere, D. A. Ritchie, E. Linfield, A. G. Davies, *et al.*, "Quantum cascade detectors," *IEEE Journal of Quantum Electronics*, vol. 45, no. 8, pp. 1039–1052, 2009.

[25] F. R. Giorgetta, E. Baumann, R. Théron, M. Pellaton, D. Hofstetter, M. Fischer, and J. Faist, "Short wavelength ($4\ \mu m$) quantum cascade detector based on strain compensated ingaas/inalas," *Applied Physics Letters*, vol. 92, no. 12, p. 121101, 2008.

[26] C. Koeniguer, L. Gendron, X. Marcadet, and V. Berger, "Characterization and modeling of a quantum cascade detector," in *Infrared Technology and Applications XXXI* (B. F. Andresen and G. F. Fulop, eds.), vol. 5783, pp. 767 – 776, International Society for Optics and Photonics, SPIE, 2005.

[27] F. Jasnot, N. Péré-Laperne, L.-A. de Vaulchier, Y. Guldner, F. Carosella, R. Ferreira, A. Buffaz, L. Doyennette, V. Berger, M. Carras, and X. Marcadet, "Photocurrent analysis of quantum cascade detectors by magnetotransport," *Phys. Rev. B*, vol. 82, p. 125447, Sep 2010.

[28] S. Saha and J. Kumar, "Rate equation modelling and investigation of quantum cascade detector characteristics," *Superlattices and Microstructures*, vol. 98, pp. 70–77, 10 2016.

[29] J. Popp, M. Haider, M. Franckié, J. Faist, and C. Jirauschek, "Monte carlo modeling of terahertz quantum cascade detectors," in *2020 XXXIIIrd General Assembly and Scientific Symposium of the International Union of Radio Science*, pp. 1–3, 2020.

[30] J. Popp, M. Haider, M. Franckié, J. Faist, and C. Jirauschek, "Monte carlo modeling of a short wavelength strain compensated quantum cascade detector," in *2021 Conference on Lasers and Electro-Optics Europe European Quantum Electronics Conference (CLEO/Europe-EQEC)*, pp. 1–1, 2021.

[31] A. Wacker, M. Lindskog, and D. O. Winge, "Nonequilibrium green's function model for simulation of quantum cascade laser devices under operating conditions," *IEEE Journal on Selected Topics in Quantum Electronics*, vol. 19, 2013.

[32] G. Bastard, "Wave mechanics applied to semiconductor heterostructures," 1990.

[33] L. Nevou, "Q_SchrodingerPoisson1D_CB." `https://github.com/LaurentNevou/Q_SchrodingerPoisson1D_CB`, 2023. GitHub. Retrieved July 6, 2023.

[34] W. Gös, *Hole trapping and the negative bias temperature instability*. PhD thesis, 2011.

[35] S.-H. Wei and A. Zunger, "Calculated natural band offsets of all II–VI and III–V semiconductors: Chemical trends and the role of cation d orbitals," *Applied Physics Letters*, vol. 72, pp. 2011–2013, 04 1998.

[36] I. Vurgaftman and J. R. Meyer, "Band parameters for nitrogen-containing semiconductors," *Journal of Applied Physics*, vol. 94, pp. 3675–3696, 9 2003.

[37] N. H. Kargan and M. K. M. Farshi, "Effect of temperature on the current–voltage characteristics of gaas/algaas quantum cascade photodetectors," *Physica E: Low-dimensional Systems and Nanostructures*, vol. 54, pp. 336–340, 2013.

[38] R. Ferreira and G. Bastard, "Evaluation of some scattering times for electrons in unbiased and biased single-and multiple-quantum-well structures," *Physical Review B*, vol. 40, no. 2, p. 1074, 1989.

[39] K. Donovan, P. Harrison, and R. W. Kelsall, "Self-consistent solutions to the intersubband rate equations in quantum cascade lasers: Analysis of a gaas/alxga1xas device," *Journal of Applied Physics*, vol. 89, pp. 3084–3090, 03 2001.

[40] B. Schwarz, P. Reininger, H. Detz, T. Zederbauer, A. Maxwell Andrews, S. Kalchmair, W. Schrenk, O. Baumgartner, H. Kosina, and G. Strasser, "A bi-functional quantum cascade device for same-frequency lasing and detection," *Applied Physics Letters*, vol. 101, no. 19, p. 191109, 2012.

[41] M. C. Sarihan, "Photonic integrated circuit components with amorphous structures," Master's thesis, Middle East Technical University, 2018.

[42] A. Gövdeli, "Integrated optical modulators based on photonic crystals," Master's thesis, Middle East Technical University, 2018.

[43] M. Erdil, "A one dimensional slot mode photonic crystal nanobeam cavity design for optical bio-sensing applications," Master's thesis, Middle East Technical University, 2020.

[44] S. C. Kılıç, "Two dimensional silicon photonic crystal band gap applications for optical bio-sensing and modulation," Master's thesis, Middle East Technical University, 2021.

[45] F. Uzgur, U. Karaca, E. Kizilkan, and S. Kocaman, "Al/sb free ingaas unipolar barrier infrared detectors," in *Infrared Technology and Applications XLIII*, vol. 10177, pp. 30–36, SPIE, 2017.

[46] A. Şahin and S. Kocaman, "Low dark current designs for mesa type swir photodetectors," in *Infrared Technology and Applications XLVI*, vol. 11407, p. 1140704, SPIE, 2020.

[47] A. Şahin, M. S. Gül, F. Uzgur, and S. Kocaman, "Dual-band ingaas nbn photodetectors at 2 μm," *Applied Physics Letters*, vol. 120, no. 9, 2022.

[48] K. Circir and S. Kocaman, "Electrical crosstalk suppression for mesa-based in-device passivated ingaas photodetectors," *Infrared Physics & Technology*, vol. 127, p. 104355, 2022.

[49] F. Uzgur and S. Kocaman, "Barrier engineering for hgcdte unipolar detectors on alternative substrates," *Infrared Physics & Technology*, vol. 97, pp. 123–128, 2019.

[50] A. Govdeli, M. C. Sarihan, U. Karaca, and S. Kocaman, "Integrated optical modulator based on transition between photonic bands," *Scientific reports*, vol. 8, no. 1, p. 1619, 2018.

[51] A. Govdeli and S. Kocaman, "Tunable integrated optical modulator with dynamical photonic band transition of photonic crystals," in *Silicon Photonics XIV*, vol. 10923, pp. 194–200, SPIE, 2019.

[52] M. Yildirim, A. Govdeli, and S. Kocaman, "Integrated optical modulators with zero index metamaterials based on photonic crystal slab waveguides," in *Integrated Optics: Devices, Materials, and Technologies XXIII*, vol. 10921, pp. 270–275, SPIE, 2019.

[53] A. Govdeli, M. C. Sarihan, U. Karaca, and S. Kocaman, "Band-to-band transition based on-chip optical modulator," in *2018 IEEE Photonics Conference (IPC)*, pp. 1–2, IEEE, 2018.

[54] U. Karaca, A. Govdeli, and S. Kocaman, "Hybrid integration of broadband silicon modulators and ingaas photodetectors," in *2018 IEEE Photonics Conference (IPC)*, pp. 1–2, IEEE, 2018.

[55] A. B. Bozkurt and S. Kocaman, "Linear optical deterministic and reconfigurable swap gate," *Quantum Information Processing*, vol. 20, pp. 1–12, 2021.

[56] Y. Basay and S. Kocaman, "Design of integrated photonic controlled-phase gate with programmable phase for quantum applications," in *Quantum Computing, Communication, and Simulation II*, vol. 12015, p. 1201503, SPIE, 2022.